

Electronic Thesis and Dissertation Repository

1-21-2019 2:30 PM

Heat of Hydration Thermal Performance and Flexural Capacity of Stainless-Steel Reinforced Concrete Sections

Mokhtar Khalifa, *The University of Western Ontario*

Supervisor: Youssef, Maged A., *The University of Western Ontario*

A thesis submitted in partial fulfillment of the requirements for the Master of Engineering Science degree in Civil and Environmental Engineering

© Mokhtar Khalifa 2019

Follow this and additional works at: <https://ir.lib.uwo.ca/etd>



Part of the [Structural Engineering Commons](#)

Recommended Citation

Khalifa, Mokhtar, "Heat of Hydration Thermal Performance and Flexural Capacity of Stainless-Steel Reinforced Concrete Sections" (2019). *Electronic Thesis and Dissertation Repository*. 5999.
<https://ir.lib.uwo.ca/etd/5999>

This Dissertation/Thesis is brought to you for free and open access by Scholarship@Western. It has been accepted for inclusion in Electronic Thesis and Dissertation Repository by an authorized administrator of Scholarship@Western. For more information, please contact wlsadmin@uwo.ca.

ABSTRACT

Stainless steel (SS) is increasingly used in the construction field due to its high strength and corrosion resistance. However, its coefficient of thermal expansion is different from that of concrete. This difference raises concerns about the potential for concrete cracking during the hydration process. To address this concern, a thermal-structural finite element model was developed to predict the stresses in SS reinforced concrete (RC) sections during the hydration process. Different curing regimes were taken into consideration. The analysis was performed in two stages. First, a transient thermal analysis was performed to determine the temperature distribution within the concrete section as a function of concrete age and its thermal properties. The evaluated temperature distribution was then utilized to conduct stress analysis. The ability of the model to predict the stresses induced by the expansion of the bars relative to the surrounding concrete was validated using relevant studies by others. The model outcomes provided in-depth understanding of the heat of hydration induced-stresses in the examined SS RC sections. Another concern for SS RC sections relates to the undefined yield point for SS. This creates uncertainty while calculating the moment of resistance of a SS RC section. An experimental-analytical study was conducted to define the SS stress corresponding the moment of resistance of beams and columns. The experimental phase involved testing four beams and four columns. Both austenitic (316 LN) and duplex (2205) were considered. A sectional analysis model was then developed, validated, and utilized to conduct a comprehensive parametric study. Expressions that allow engineers to accurately estimate the moment of resistance of SS RC sections were developed.

Keywords: Concrete; Stainless Steel; Reinforcement; Temperature; Yield Stress.

CO-AUTHORSHIP STATEMENT

All the experimental and analytical work presented in this thesis was performed by Mokhtar Khalifa. Chapters 3, 4 of this thesis will be submitted to scholarly journals as manuscripts co-authored by Mokhtar Khalifa, Dr. Monir Ajan Alhadid and Prof. Maged Youssef. The following publication was drafted by the authors and reviewed and edited by Prof. Maged Youssef:

Khalifa, Mokhtar A., Alhadid, Monir M., Youssef, Maged A. (2018) “Early Age Thermal Expansion of Stainless-Steel Reinforced Concrete Sections”. Proceedings of the 10th International Conference on Short and Medium Span Bridges, Quebec City, Quebec, Canada.

ACKNOWLEDGMENTS

This research would have not been possible without the financial support of the Ministry of Transportation of Ontario (MTO). I also like to thank Salit Specialty Rebar that donated the Stainless-Steel material essential for the experimental work.

I would like to express my greatest appreciation to my supervisor Prof. Maged Youssef for his enthusiastic encouragement, continuous guidance and patience during my master study. His support and immense knowledge helped me in all the time of research. I could not have imagined having better supervisor during my research.

I have special gratitude to Dr. Monir Elhadid whose persistent help, personal, and professional experience in research and life helped me a lot more than I can give him credit for.

My genuine thanks go to Dr. Aiham Adawi for his great assistance in preparing the experimental setup. I would also like to thank my friends who helped me during the concrete casting, specially Mohammad Noor Tamim, Rob Keuhnen, Murad Ilomame, Emad Abraik and Moustafa Aboutabikh.

Finally, thanks to my family for their constant prayers that supported me spiritually through my research and life.

TABLE OF CONTENTS

ABSTRACT	i
CO-AUTHORSHIP STATEMENT	ii
ACKNOWLEDGMENTS	iii
TABLE OF CONTENTS	iv
LIST OF TABLES	viii
LIST OF FIGURES	ix
LIST OF APPENDICES	xii
LIST OF ABBREVIATIONS AND SYMBOLS	xiii
Chapter 1	1
1. INTRODUCTION	1
1.1. General	1
1.2. Objectives	2
1.3. Scope of the thesis	3
1.4. References	4
Chapter 2	6
2. LITERATURE REVIEW	6
2.1. Introduction	6
2.2. Stainless Steel Reinforcement	6
2.2.1. Stainless Steel Classification	7
2.2.2. Thermal and Mechanical Properties of Stainless Steel	8
2.2.3. Uses of Stainless Steel	11
2.3. Concrete	13
2.3.1. Heat of Hydration	13
2.3.2. Thermal and Mechanical Properties	15

2.3.3. Sensitivity of Moment of Resistance to Steel Yield Strength	16
2.4. Summary	17
2.5. References	18
Chapter 3	21
3. HEAT OF HYDRATION INDUCED STRESSES IN STAINLESS-STEEL REINFORCED CONCRETE SECTIONS	21
3.1. Introduction	21
3.2. Material Models	22
3.2.1. Concrete	22
3.2.2. Stainless Steel Bars	25
3.3. Finite Element Model.....	25
3.3.1. Thermal Analysis.....	26
3.3.2. Structural Analysis Model	28
3.4. Validation	29
3.5. Parametric Study	32
3.6. Summary and Conclusions	41
3.7. References	42
Chapter 4	44
4. PREDICTING THE FLEXURAL CAPACITY OF STAINLESS-STEEL REINFORCED CONCRETE SECTIONS CONSIDERING THE AXIAL LOAD LEVEL	44
4.1. Introduction	44
4.2. Experimental Program	45
4.2.1. Tensile Tests on Stainless-Steel Bars	45
4.2.2. Large-Scale Tests Performed on Beams	46
4.2.3. Large-Scale Tests Performed on Columns	50
4.3. Discussion of the Experimental Results.....	52

4.3.1. Tensile Tests on Stainless-Steel Bars	53
4.3.2. Large-Scale Tests Performed on Beams	54
4.3.3. Large-Scale Tests Performed on Columns	62
4.4. Analytical Model	68
4.4.1. Assumptions.....	69
4.4.2. Material Models.....	69
4.4.3. Sectional Analysis	70
4.5. Validation of the Analytical Model.....	72
4.5.1. Beams	72
4.5.2. Columns	74
4.6. Parametric Study	76
4.7. Effect of the Examined Parameters on Stainless-Steel RC Beams.....	79
4.7.1. Effect of Section Height (h)	79
4.7.2. Effect of Section Width (b).....	80
4.7.3. Effect of Reinforcement Ratio (ρ)	80
4.8. Effect of the Examined Parameters on Stainless-Steel RC Columns	82
4.8.1. Effect of Section Height (h)	82
4.8.2. Effect of Section Width (b).....	83
4.8.3. Effect of Reinforcement Ratio (ρ)	85
4.9. Proposed Procedure to Calculate the Flexural Capacity of Stainless-Steel RC Members.....	86
4.10. Summary and Conclusions	90
4.11. References.....	96
5. CONCLUSION	98
5.1. Summary	98
5.2. Conclusions.....	99

5.2.1. Properties of Stainless-Steel Reinforced Sections during Early Hydration Process	99
5.2.2. Flexural Performance of Stainless-Steel Reinforced Concrete Sections	100
5.3. Recommendations	101
CURRICULUM VITAE.....	102

LIST OF TABLES

Table 4.1: Description of the Beam Specimens	47
Table 4.2: Description of the Column Specimens	50
Table 4.3: Dimensions and Reinforcement Ratios of the Beam Specimens.....	77
Table 4.4: Dimensions and Reinforcement Ratio of the Column Specimens.....	78

LIST OF FIGURES

Figure 2.1: Typical Stress-Strain Curve of Stainless-Steel.....	10
Figure 2.2: Stress-Strain Curves for Austenitic 304 SS.....	10
Figure 2.3: Stonecutters Bridge, Hong Kong [12]	12
Figure 2.4: Broadmeadow Bridge [13].....	12
Figure 2.5: Sheik Zayed Bridge, Abu Dhabi [12].....	13
Figure 2.6: Stages of Heat of Hydration [18,19].....	15
Figure 2.7: Effect of Varying Steel Yield Strength on Concrete Section Moment of Resistance	17
Figure 3.1: Variation of Concrete Strength with Time.....	23
Figure 3.2: Stress-Strain Curves of Concrete at Early Age	24
Figure 3.3: Thermal Conductivity for Concrete at Different Temperatures.....	25
Figure 3.4: Typical SS RC Section.....	26
Figure 3.5: Thermal Analysis Mesh	27
Figure 3.6: Heat of hydration at Different Ages [17, 20].....	28
Figure 3.7: Structural Finite Element Model	29
Figure 3.8: Cracking of concrete due to radial expansion a cover equal to the bar diameter. .	31
Figure 3.9: Radial Expansion at Cracking	32
Figure 3.10: Variation of maximum Hydration Temperature with Time	34
Figure 3.11: Temperature Variation after 1 Day for D20-C600.....	35

Figure 3.12: Maximum Tensile Principal Stresses at Various Ages	36
Figure 3.13: Tensile Stress Contours after 1 Day for D20-C300.....	37
Figure 3.14: Maximum Compressive Principal Stresses at Various Ages	39
Figure 3.15: Radial Thermal Expansion of SS bars at Different Ages.....	40
Figure 4.1: Tensile test of the Stainless-Steel Bars	46
Figure 4.2: Cross-Sectional Details of the Tested Beams	47
Figure 4.3: Fabrication and Testing of the Beam Specimens.	49
Figure 4.4: Cross-Sectional Details of the Tested Columns	51
Figure 4.5: Steel Cages of the Tested Columns	51
Figure 4.6: Test Setup for the SS Columns.....	52
Figure 4.7: Stress-Strain Curves of the Experimentally Tested Stainless Steel Bars.....	53
Figure 4.8: Load-Deflection Curves of the Tested Beams	55
Figure 4.9: Typical Failure Mode of the Tested Beams	57
Figure 4.10: Cracking Pattern of the Tested Beams at Failure	57
Figure 4.11: Strain Profile at Mid-Span Section of the Tested Beams.....	60
Figure 4.12: Strain Variation with Load at Mid-Span Section of Beam B4.....	61
Figure 4.13: Load-Deflection Curves of the Tested Columns.	63
Figure 4.14: Typical Failure Mode of Column C1	64
Figure 4.15: Cracking Pattern of the Tested Columns at Failure.....	65
Figure 4.16: Strain Profile at Mid-Height Section of the Tested Columns.	66

Figure 4.17: Variation of Strain in the Bars with Deflection at the Mid-Height Section.....	68
Figure 4.18: Typical Mesh for the Sectional Analysis Method	71
Figure 4.19: Validation of the Proposed Analytical Model with the Experimental Results ..	73
Figure 4.20: Validation of the Proposed Analytical Model with the Experimental Results ..	75
Figure 4.21: Influence of Various Parameters on the Tensile Stress in the SS Bars at M_R	81
Figure 4.22: Influence of Varying h on f_{ss} in Stainless-Steel RC Columns.....	83
Figure 4.23: Influence of Varying b on f_{ss} in Stainless-Steel RC Columns.....	84
Figure 4.24: Influence of Varying ρ on f_{ss} in Stainless-Steel RC Columns.....	85
Figure 4.25: Accuracy of Predicting M_R for Experimentally Tested Beams	88
Figure 4.26: Accuracy of Predicting M_R for Experimentally Tested Columns	89
Figure 4.27: Accuracy of M_R for Parametric Study Sections.....	89

LIST OF APPENDICES

Appendix A.....	91
Appendix B.....	93

LIST OF ABBREVIATIONS AND SYMBOLS

A_s	Area of steel reinforcement
a	Depth of the compression block in rectangular reinforced concrete sections
b	Section width
c	Concrete cover
C_c	Concrete compressive force
C_s	Steel compressive force
d	Bar diameter
E	Stainless-steel modulus of elasticity
E_o	Stainless-steel initial modulus of elasticity
$E_{0.2}$	Stainless-steel tangent modulus of elasticity at 0.2% proof stress
e, m	Rasmussen equation parameters
f_c	Concrete stress corresponding to a strain value of ϵ_c
f'_c	Concrete compressive strength
f_t	Concrete tensile strength
f_{ss}	Equivalent stainless-steel proof stress
f_{ss}'	Compression stainless-steel proof stress
f_y	Yield strength of steel
h	Section height
h'	Section width measured to outside of the transverse reinforcement.

i, j, k	Macdonald equation parameters
K_h	Confinement factor
M_r	Moment of resistance of the reinforced concrete section
n	Ramberg-Osgood equation parameter
P_c	Axial capacity of the reinforced concrete section
P_e	Axial Load applied experimentally
S_h	Centre to centre spacing of the transverse reinforcement
T	Temperature
T_s	Tensile force in the steel bars
Z	Slope of the decaying branch of the concrete stress–strain curve
α	Parameter representing the ratio of average stress in rectangular compression stress block to the concrete compressive strength
ε	Stainless-steel strain
ε_o	Concrete strain at peak stress
$\varepsilon_{0.2}$	Stainless-steel strain corresponding to $\sigma_{0.2}$
ε_c	Concrete strain
ε_{cr}	Creep strain of concrete at maximum stress
ε_{cu}	Concrete ultimate strain
ε_{oc}	Concrete Strain at maximum stress
ε_u	Ultimate stainless-steel strain

ε_{50h}	Strain component that gives the additional ductility due to rectangular transverse reinforcement
ε_{50u}	Strain component that considers effect of concrete strength on the slope of the descending branch of concrete
λ	Axial load level
ρ	Section reinforcement ratio
ρ_s	Ratio of the volume of transverse reinforcement to the volume of concrete core measured to the outside of the transverse reinforcement.
σ	Stainless-steel stress
$\sigma_{0.01}$	0.01% stainless-steel proof stress
$\sigma_{0.2}$	0.2% stainless steel proof stress
σ_c	Concrete stress
σ_u	Ultimate stainless-steel stress
Φ	Stirrup diameter

Chapter 1

1. INTRODUCTION

1.1. General

Stainless-steel was first produced in Germany and the UK in 1912 [1]. It was termed rustless steel due to its high resistance to corrosion as compared to carbon steel. Chromium constitutes about 10% of its content, which leads to the formation of a self-healing oxide layer [2]. Stainless-steel can tolerate chloride levels up to 7% as compared to 0.4% tolerated by carbon steel. Two types of stainless-steel bars are readily available in the construction market: Austenitic and Duplex stainless-steel. Typical stainless-steel grades are 2205 for duplex stainless-steel and 316 LN for austenitic stainless-steel.

Stainless-steel bars are being used in elements that are susceptible to corrosion especially in bridges. They have also been used to retrofit existing structures, as in the cases of Leeds bridge in UK, and Progreso bridge in Mexico [3].

Carbon steel has a coefficient of thermal expansion of $1.2 \times 10^{-5} \text{ }^\circ\text{C}^{-1}$ that is close to the concrete coefficient ($1.1 \times 10^{-5} \text{ }^\circ\text{C}^{-1}$). This indicates a perfect thermal compatibility between both materials. Austenitic stainless steel has a coefficient of thermal expansion of about $1.8 \times 10^{-5} \text{ }^\circ\text{C}^{-1}$, which is higher than the concrete coefficient [4]. This difference is reduced for duplex stainless steel, which has a coefficient of thermal expansion of $1.3 \times 10^{-5} \text{ }^\circ\text{C}^{-1}$. The difference in the coefficient of thermal expansion between stainless steel and concrete causes thermal incompatibility, which may lead to crack formation. The potential for these cracks is higher during the hydration process, which causes the concrete temperature to increase, reaching

values of up to 55 °C. This increase in temperature happens, when the concrete is still developing its strength.

Carbon steel stress-strain relationship is characterized by a linear relationship followed by a well-defined yield point. On the other hand, stainless-steel stress-strain curve does not have a definite yield point [1]. The 0.2% offset strain method is currently being used to define its yield point. Design based on this point is expected to be overconservative.

Ministry of Transportation of Ontario (MTO) started using stainless steel reinforcement in bridge decks and in components subjected to salt splashing in the early 2000's. However, the Canadian Highway Bridge Design Code (CSA-S6 2015) does not have provisions for stainless steel reinforcement. This has led engineers to use design methods for carbon steel, while designing stainless-steel concrete sections. The errors associated with such designs are unknown.

1.2. Objectives

This study involves experimental, numerical and analytical methods to solve two of the issues related to the use of stainless steel to reinforce concrete members. The two issues are the thermal incompatibility between austenitic stainless steel and concrete, and the undefined yield stress of stainless steel. The thesis addresses the following objectives:

- 1- Conduct a literature review that relates to the thesis scope.
- 2- Develop a numerical model to analyze the thermal behavior of stainless-steel reinforced concrete sections during the hydration process and to investigate the potential of crack formation at this stage.

- 3- Perform individual axial tensile tests on different sizes of stainless-steel bars to evaluate their mechanical properties.
- 4- Perform experimental tests on full-scale stainless steel reinforced concrete short columns and beams to identify the stainless-steel stress corresponding to the ultimate moment.
- 5- Develop and validate a sectional analysis model to evaluate the moment of resistance of stainless-steel reinforced concrete sections.
- 6- Conduct a parametric study to examine the value of the stainless-steel stress corresponding to ultimate flexural capacity considering different section dimensions, reinforcement ratios, and concrete properties.
- 7- Propose a design method for flexural concrete members reinforced with stainless-steel bars, that is based on the stainless-steel stress at failure of the concrete section.

1.3. Scope of the thesis

The thesis is divided into five chapters that cover the literature review, the experimental work and the numerical analysis.

Chapter 1 presents an overall introduction of the thesis in terms of general background, research objectives and scope of the thesis.

Chapter 2 provides a literature review discussing stainless steel classification, uses and applications, mechanical and physical properties, stress-strain relationship, and the heat of hydration inside concrete.

Chapter 3 presents the details of the numerical model that evaluates the temperature distribution within concrete as a result of heat of hydration, examines the stresses induced due to the thermal

incompatibility between stainless-steel and concrete, and examine the potential of cracks at this stage.

Chapter 4 provides details of the experimental program that involved performing tensile tests on stainless-steel bars and conducting large-scale tests on stainless-steel reinforced concrete beams and columns. The sectional analysis method is then presented, validated and utilized to conduct a parametric study. Equations defining the stainless-steel stress at failure are then proposed and validated.

Chapter 5 provides the overall conclusions of the research as well as recommendations for future work.

1.4. References

- [1] Gardner, L. 2005. The Use of Stainless Steel in Structures. *Progress in Structural Engineering and Materials*. 7(2): 45-55.
- [2] Baddoo, N. R. 2008. Stainless Steel in Construction: A Review of Research, Applications, Challenges and Opportunities. *Journal of Construction Steel Research*. 64: 1199-1206.
- [3] Castro-Borges, P & Rincon, Oladis & Moreno, E.I. & Torres-Acosta, Andres & Martínez-Madrid, M & Knudsen, Asger. (2002). Performance of a 60-year-old concrete pier with stainless steel reinforcement. *Materials Performance*. 41: 50-55.
- [4] Nürnberger, U. 2005. Stainless steel reinforcement - a survey. *Otto Graf Journal*. 16:111-138.

Chapter 2

2. LITERATURE REVIEW

2.1. Introduction

Corrosion of carbon steel is a major problem in RC structures. Stainless steel bars present a feasible solution for this problem. However, such solution requires understanding of the potential issues associated with stainless-steel bars. Two of the known issues are linked to their thermal characteristics and undefined yield stress. This chapter presents a background related to the aforementioned issues.

2.2. Stainless Steel Reinforcement

The term stainless steel does not refer to single metal. Instead it is used for a group of corrosion-resistant alloys. The primary alloy in stainless steel is chromium with a minimum content of 10.5%. It forms a chromium-oxide layer on the bar surface that provides corrosion protection. If this protective layer is damaged, oxygen enables its self-healing [1]. Corrosion resistance can be further improved by adding other alloys including chromium, nitrogen, molybdenum, titanium and nickel, which makes stainless steel suitable for use in acid media [2]. Other alloys include: carbon and manganese. Manganese improves hot working properties, strength, and toughness [3]. The composition of stainless-steel bars defines their corrosion resistance, mechanical properties, and weldability [2].

2.2.1. Stainless Steel Classification

Three types of stainless-steel bars are readily available in the construction market. These are austenitic, ferritic, and ferritic-austenitic (duplex).

Ferritic stainless steel has chromium content of about 30% and is characterized by possessing ferromagnetic properties. Its tensile strength is higher than that of austenitic stainless steel, but its workability is not as efficient as other types. It is not recommended to be used for applications requiring long-life span or exposure to chloride ions [2].

Austenitic stainless steel has 17 to 25 % chromium and 8 to 26 % nickel. It has excellent toughness, ductility and weldability as compared to both ferritic and duplex stainless steel. Additionally, its high ductility has promoted its use in seismic areas. Austenitic stainless steel is available as low-carbon chromium-nickel alloy (grades 304, 304L, 316, and 316L), which contains up to 0.3% carbon. It is used in chloride environment. It is also available as chromium-manganese-nitrogen alloy [2].

Ferritic-austenitic (duplex) stainless steel has a binary structure of ferrite and austenite. It contains up to 8% nickel, and between 22 and 28% chromium. Molybdenum improves its corrosion resistance. It has improved ductility and toughness as compared to ferritic stainless-steel, and has improved strength, and corrosion resistance as compared to both austenitic and ferritic stainless steel [1]. Duplex stainless-steel grades include: 2205, 2304 and 2507.

2.2.2. Thermal and Mechanical Properties of Stainless Steel

The electrical resistivity and thermal conductivity of carbon steel and stainless steel are different [2,4]. However, they are similar in terms of modulus of elasticity and density. In terms of thermal behavior, ferritic, austenitic and duplex stainless-steel bars have thermal conductivity of 23 W/m.°C, 15 W/m.°C and 20 W/m.°C respectively [2]. Duplex, ferritic and austenitic stainless-steel have coefficients of thermal expansion of $13 \times 10^{-6} \text{ }^\circ\text{C}^{-1}$, $12 \times 10^{-6} \text{ }^\circ\text{C}^{-1}$, and $17.8 \times 10^{-6} \text{ }^\circ\text{C}^{-1}$, respectively [4]. However, carbon steel has thermal conductivity of 36 W/m.°C, and coefficient of thermal expansion of $12 \times 10^{-6} \text{ }^\circ\text{C}^{-1}$ [2].

Typical stress-strain (σ - ε) curves of stainless-steel bars do not show a well-defined yield point as illustrated in Fig. 2.1. Engineers tend to use the 0.2% proof stress as the yield strength [2].

Ramberg-Osgood [5] developed an expression that can be used to describe the stress-strain behavior of stainless-steel bars as shown in Equation 2.1. The expression is defined in terms of a calibration parameter (n), a proof stress ($\sigma_{0.2}$) as defined in Fig. 2.1, and an initial modulus of elasticity (E_o).

$$\varepsilon = \frac{\sigma}{E_o} + 0.002 \left(\frac{\sigma}{\sigma_{0.2}} \right)^n \quad (2.1)$$

Macdonald [6] performed experimental tests on columns reinforced with 304 Austenitic stainless-steel. The accuracy of Ramberg-Osgood stress-strain curve was found to significantly decrease at strains higher than 0.2% of the total strain. Macdonald proposed a new stress-strain expression to address this issue Equation 2.2 [5]. The developed expression proved to be accurate for 304 Austenitic stainless steel [6].

$$\varepsilon = \frac{\sigma}{E_o} + 0.002 \left(\frac{\sigma}{\sigma_1} \right)^{(i+j) \left(\frac{\sigma}{\sigma_1} \right)^k} \quad (2.2)$$

Constants i , j and k range between 2.5 and 6 depending on the stainless-steel thickness.

Based on experimental study, Olsson [7] recommended using Equation 2.1 for stresses less than or equal $\sigma_{0.2}$ then a straight line for higher stresses. Rasmussen [8] also used Equation 2.1 for stresses less than or equal to $\sigma_{0.2}$ and Equation 2.3 for higher stresses.

$$\varepsilon = \frac{\sigma - \sigma_{0.2}}{E_{0.2}} + \varepsilon_u \left(\frac{\sigma - \sigma_{0.2}}{\sigma_u - \sigma_{0.2}} \right)^m + \varepsilon_{0.2} \quad \text{for } \sigma > \sigma_{0.2} \quad (2.3)$$

where: σ is the stress, n is a parameter which determines the sharpness of the stress strain curve and can be calculated using this equation: $n = \frac{\ln(20)}{\ln(\sigma_{0.2}/\sigma_{0.01})}$, m can be obtained from the equation: $m = 1 + 3.5 \frac{\sigma_{0.2}}{\sigma_u}$, ε is the strain, $\sigma_{0.01}$ is the 0.01% proof stress, E_o is the initial modulus to the curve, $E_{0.2}$ is the tangent modulus of the stress–strain curve at the 0.2% proof stress calculated using this equation: $E_{0.2} = \frac{E_o}{1 + 0.002n/e}$, $\sigma_{0.2}$ is the 0.2% proof stress, e is a non-dimensional proof stress parameter and can be calculated using this equation: $e = \frac{\sigma_{0.2}}{E_o}$, $\varepsilon_{0.2}$ is the 0.2% total strain, and can be calculated using this equation: $\varepsilon_{0.2} = \frac{\sigma_{0.2}}{E_o} + 0.002$, σ_u is the ultimate stress, ε_u is the ultimate strain.

Fig. 2.2 shows the stress-strain curve of austenitic stainless-steel grade 304 sketched using different models. The used parameters are $\sigma_{0.2} = 532$ MPa, $\sigma_{0.01} = 297$ MPa, $E_o = 182,000$ MPa, $i = 6$, $j=5$, and $k=3$.

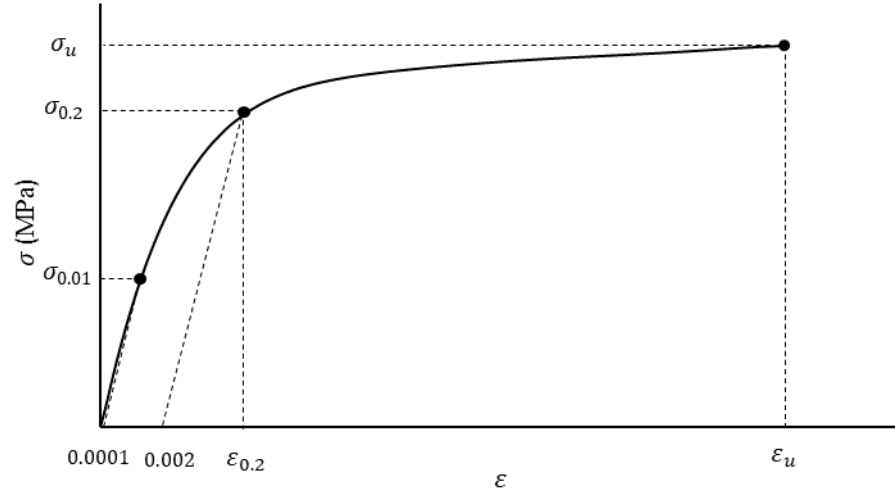


Figure 2.1: Typical Stress-Strain Curve of Stainless-Steel

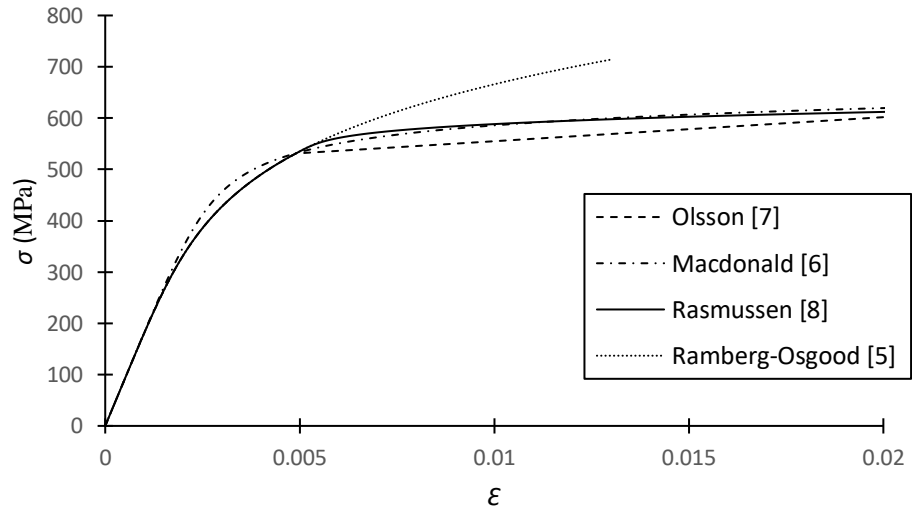


Figure 2.2: Stress-Strain Curves for Austenitic 304 SS

2.2.3. Uses of Stainless Steel

The use of stainless-steel bars as reinforcement in concrete structures are addressed by two main standards: ASTM A955M-18 [9] and BS 6744 [10]. Both standards cover mechanical properties, bond classification, chemical analysis, and strength of stainless steel.

One of the early examples for using corrosion resistant steel in concrete is the Progresso pier which was constructed in 1940 in the Gulf of Mexico [11]. Over the last 20 years, use of stainless steel has increased in coastal structures, buildings, and bridges. Examples for stainless steel use include Celtic gateway footbridge in UK, Stonecutters bridge in Hong Kong (Fig. 2.3) [12], Highnam Bridge in UK, Broadmeadow Bridge in Ireland (Fig. 2.4) [13], Sheikh Zayed bridge in UAE (Fig. 2.5) [12], and Belt Parkway Bridge in USA [14]. Due to the nonmagnetic properties of austenitic stainless-steel bars, it is widely used in the X-ray units in hospitals and medical centers [15]. It has also been used for retrofitting historical buildings such as the Cathedral of Milan in Italy, the Coliseum in Italy, and Guildhall building in UK. It has been used in retrofitting coastal structures including the replacement of parts of the seawall of Sydney Harbour in Australia [12].

The main issue preventing the wide use of stainless steel is the material cost. However, if maintenance and life cycle costs are accounted for, stainless-steel use can be justified. Additionally, the fact that current design standards do not differentiate between carbon steel and stainless steel is disadvantageous for stainless-steel. Changes to account for the higher corrosion resistance of stainless steel are expected to include concrete mix design, concrete cover, use of waterproofing membranes, and crack width limits [4].



Figure 2.3: Stonecutters Bridge, Hong Kong [12]



(a) Bridge photo



(b) Detail of stainless-steel column mesh

Figure 2.4: Broadmeadow Bridge [13]



Figure 2.5: Sheik Zayed Bridge, Abu Dhabi [12]

2.3. Concrete

2.3.1. Heat of Hydration

The chemical reaction between cement and water determines the setting and hardening properties of concrete. This section discusses the process of hydration of Portland cement.

Ordinary Portland Cement is the most used cement in concrete structures. Its main components are: Belite (C_2S), aluminate (C_3A), alite (C_3S), and tetra calcium aluminoferrite (C_4AF) [16]. Hydration products are formed when water and cement components are mixed together. Calcium silicates consist of tricalcium silicate (C_3S) and dicalcium silicate (C_2S). Hydration reactions of both calcium silicates produce calcium hydroxide and calcium silicate hydrate (C-S-H) [16].

Ettringite and monosulfoaluminate are the hydration products of C_3A . The formation of ettringite contributes to early strength development. After the depletion of sulfate in the chemical reaction, ettringite becomes unstable and is gradually converted into monosulfoaluminate. If a new source of sulfate is added, monosulfoaluminate is converted back to ettringite. The hydration products of both C_3A and tetra calcium aluminoferrite (C_4AF) are similar [16].

The cement hydration process releases heat that was recorded by Lerch [17]. The released heat can be divided into five stages as shown in Fig. 2.6 [16]. In Stage I (the dissolution stage), the hydration reaction starts for C_3A , and Ettringite is formed. In Stage II (the induction [dormant] period), this stage is vital for concrete workability. Concrete does not develop any strength at this stage. In Stage III (the acceleration stage), C_3S and C_2S hydrate and release heat. Therefore, concrete develops its strength. In stage IV (the deceleration stage), C_3A hydration process leads to the conversion of Ettringite to monosulfate. Heat generation rate decreases during this stage and cement acts as a diffusion layer. In stage V (the steady stage), rate of hydration is slowed down significantly due to the thick layer of hydrates around cement.

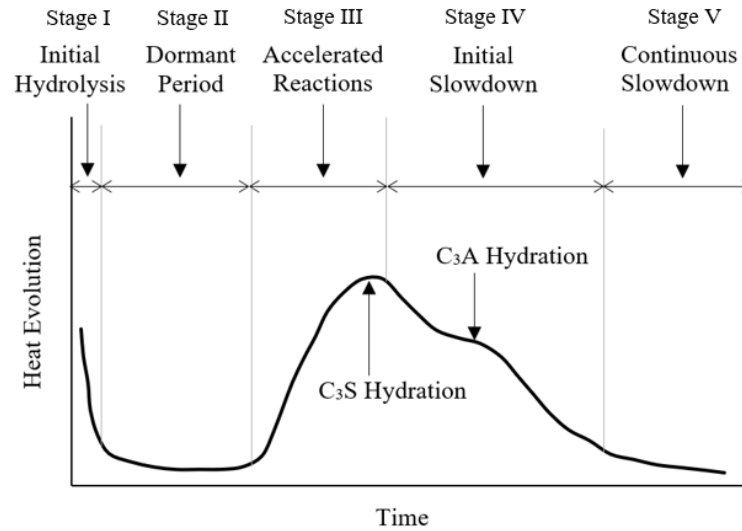


Figure 2.6: Stages of Heat of Hydration [18,19]

2.3.2. Thermal and Mechanical Properties

Thermal conductivity of concrete ranges between 1.15 and 1.5 W/m^oK at room temperature and varies with temperature [20]. The specific heat of concrete varies from 840 J/kg. K to 1800 J/kg. K at room temperature. Its value depends on the moisture content [21]. Thermal expansion of concrete is a function of concrete age, water content, cement type, aggregate type, and temperature [22]. Compressive strength of normal strength concrete varies from 20 to 80 MPa [23]. The tensile strength is about 10 to 15% of the compressive strength. The modulus of elasticity of concrete varies from 5.0×10^3 to 35.0×10^3 MPa at room temperature, and depends on the age of concrete, water-cement ratio, amount and nature of the aggregates [24]. Concrete mechanical response is usually expressed in the form of stress-strain relationships, which are mainly dependent on the concrete strength [18]. Kent and Park [25] developed a concrete stress-stress model described in Eq. (2.5 a-f) that considers ductility improvement provided by rectangular hoops.

$$f_c = K_h f'_c \left[2.0 \left(\frac{\varepsilon_c}{\varepsilon_{oc} + \varepsilon_{cr}} \right) - \left(\frac{\varepsilon_c}{\varepsilon_{oc} + \varepsilon_{cr}} \right)^2 \right] \quad \varepsilon_c < \varepsilon_{oc} + \varepsilon_{cr} \quad (2.4a)$$

$$K_h = 1 + \frac{\rho_s f_y}{f'_c} \quad (2.4b)$$

$$Z = \frac{0.5}{\varepsilon_{50u} + \varepsilon_{50h} - \varepsilon_o - \varepsilon_{cr}} \quad (2.4c)$$

$$\varepsilon_{50u} = \frac{3 + 0.29 f'_c}{145 f'_c - 1000} + \varepsilon_{cr} \quad (2.4d)$$

$$\varepsilon_{50h} = 0.75 \rho_s \sqrt{\frac{h'}{s_h}} \quad (2.4e)$$

$$f_c = K_h f'_c [1 - Z(\varepsilon_{50h} - \varepsilon_o - \varepsilon_{cr})] \geq 0.2 K_h f'_c \quad \varepsilon_c < \varepsilon_{oc} + \varepsilon_{cr} \quad (2.4f)$$

Where, K_h is a confinement factor, f'_c is concrete compressive strength, ρ_s is ratio of the volume of transverse reinforcement to the volume of concrete core measured to their outer perimeter, ε_c is concrete strain, f_y is yield strength of reinforcement, ε_{oc} is the concrete strain at maximum stress ($\varepsilon_{oc} = \varepsilon_o \times K_h$), Z is the slope of the decaying branch, S_h represents centre-to-centre spacing of the transverse reinforcement, and h' is the width of the concrete core measured to outside of the transverse reinforcement.

2.3.3. Sensitivity of Moment of Resistance to Steel Yield Strength

Moment of resistance of reinforced concrete sections is highly affected by the steel yield strength. To clarify this fact, a concrete section of width 250 mm and depth 510 mm is assumed. The section is reinforced with 2M25. f'_c (compressive strength of concrete) is 30 MPa. Varying f_y (yield strength of steel) from 300 MPa to 500 MPa results in significant variation in the

moment of resistance as shown in Fig. 2.7. Thus, it is critical to have an accurate value for f_y while calculating M_r (concrete section moment of resistance).

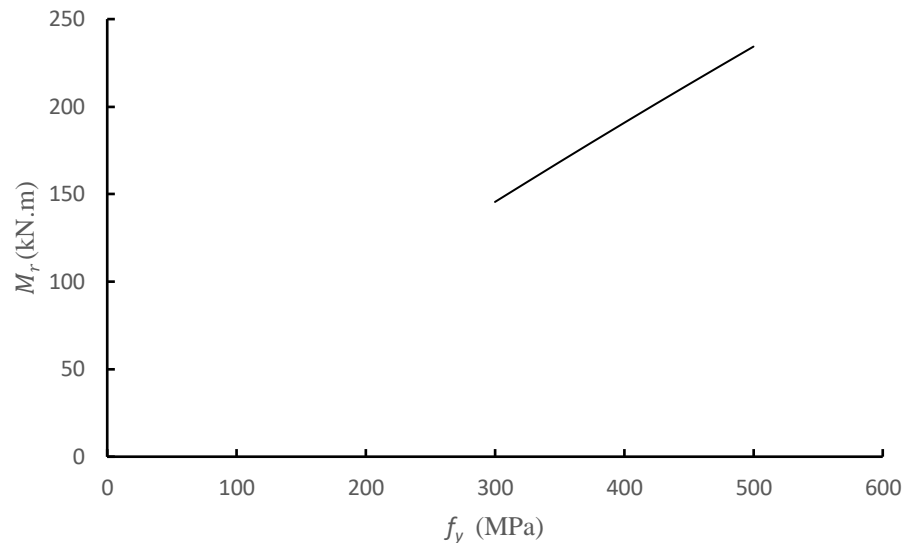


Figure 2.7: Effect of Varying Steel Yield Strength on Concrete Section Moment of Resistance

2.4. Summary

This chapter discussed background information for two concerns related to using stainless steel bars in concrete structures. Regarding stainless-steel, the presented information covered alloys, thermal properties, mechanical properties, and applications in construction. Concrete properties were then mentioned, and heat of hydration reactions were explained. The sensitivity of the moment of resistance of concrete sections to variations in the yield strength was also discussed.

2.5. References

- [1] Stainless Steels, 1994, ASM Specialty Handbook: Stainless Steels, edited by J. R., Davis ASM International, Ohio, USA, 576 p.
- [2] Nürnberger, U. 2005. Stainless steel reinforcement - a survey. *Otto Graf Journal*. 16: 111-138.
- [3] Cunat, P. 2004. Alloying Elements in Stainless Steel and Other Chromium-Containing Alloys. International Chromium Development Association, Paris, France, 24 p.
- [4] Soudki, K.A, West, J.S, Campbell T.I, 2004. Effect of Temperature on Structural Performance of Stainless-Steel Reinforcement, MTO, Waterloo, Ontario, Canada, 82 p.
- [5] Ramberg, W., Osgood, W. 1943. Description of Stress–Strain Curves by Three Parameters. Technical Note No. 902, National Advisory Committee for Aeronautics. Washington, D.C, USA, 29 p.
- [6] MacDonald M, Rhodes J, Taylor GT. 2000. Mechanical properties of stainless-steel lipped channels. In: LaBoube RA, Yu W-W. Proceedings, 15th International Specialty Conference on Cold Formed Steel Structures. University of Missouri-Rolla, USA; pp. 673–86.
- [7] Olsson A. 2001. Stainless steel plasticity—material modelling and structural applications. PhD thesis, Department of Civil and Mining Engineering, Lulea University of Technology, Sweden. 298 p.
- [8] Rasmussen, K.J.R. 2003. Full Range Stress–Strain Curves for Stainless Steel Alloys. *Journal of Constructional Steel Research*. 59: 47–61.
- [9] A955M-18, 2018, Standard Specification for Deformed and Plain Stainless-Steel Bars for Concrete Reinforcement, ASTM International, West Conshohocken, PA, USA, 14 p.
- [10] BS 6744. 2016. Stainless steel bars. Reinforcement of concrete. Requirements and test methods, BSI, Sheffield, UK, 44 p.

- [11] The Concrete Society, 1998, "Guidance on the use of stainless-steel reinforcement", The Concrete Society Technical Report 51, Slough, Berkshire, UK, 55 p.
- [12] Markest, G. Rostam, S. and, 2006, Guide for the use of stainless-steel reinforcement in concrete structures, Klinghoffer, O., Norwegian Building Research Institute, Oslo, Norway, 59 p.
- [13] British Stainless-Steel Association. 2003, The Use of Stainless-Steel Reinforcement in Bridges. Sheffield, UK, 4 p.
- [14] Annan, C. 2013. Relevance of Traditional Steel Design and Fabrication Requirements to Structural Stainless Steels. *Advances in Structural Engineering*. 16(3): 517-528.
- [15] Baddoo, N. R. 2008. Stainless Steel in Construction: A Review of Research, Applications, Challenges and Opportunities. *Journal of Construction Steel Research*. 64: 1199-1206.
- [16] Zhi, G. 2005. Predicting Temperature and Strength Development of the Field Concrete, PhD. Dissertation, Iowa State University, Ames, Iowa, USA, 233 p.
- [17] Metha, P.K., and Paulo J.M. Monteiro. (2006). *Concrete, Microstructure, Properties, and Materials*. McGraw-Hill Company, Inc, New York, NY, USA, 659 p.
- [18] Byfors, J. 1980. *Plain Concrete at Early Ages*. Swedish Cement and Concrete. Stockholm, Sweden, 464 p.
- [19] Mindess, S. Young, J.F. and Darwin, D. (2002). *Concrete*. 2nd Edition, Pearson Education, Inc, Upper Saddle River, New Jersey, USA. 644 p.
- [20] Background Documents to EN 1992-1-2 Eurocode 2: Design of concrete structures Part 1-2: General rules – Structural fire design, CEN, Brussels, Belgium
- [21] Kodur, V. 2014. *Properties of Concrete at Elevated Temperatures*. ISRN Civil Engineering. Hindawi Publishing Corporation, Cairo, Egypt. 15 p.
- [22] Bazant Z.P., and Chern J.C., 1987, "Stress-induced thermal and shrinkage strains in concrete," *Journal of Engineering Mechanics*, 113(10): 1493–1511.

- [23] CSA A23.3. 2014. Design of concrete structures. Cement Association of Canada, Ottawa, ON, Canada, 297 p.
- [24] Cruz, C.R., 1966, "Elastic properties of concrete at high temperatures," Journal of the PCA Research and Development Laboratories, 8: 37–45.
- [25] Kent DC, Park R, 1971. Flexural members with confined concrete. Journal of the Structural Division; 97(7):1969–1990.

Chapter 3

3. HEAT OF HYDRATION INDUCED STRESSES IN STAINLESS-STEEL REINFORCED CONCRETE SECTIONS

3.1. Introduction

Stainless steel (SS) provides many advantages over conventional carbon steel due to its high corrosion resistance, and consequently its lower dependency on the alkalinity of the protective concrete cover. Using SS bars to reinforce concrete structures results in a significant improvement in their durability and reduction in their maintenance and repair cost. As such, the use of SS bars in the construction industry continues to increase, especially in bridges and coastal structures [1].

Despite the various pros of SS bars, their thermal properties constitute a drawback. The reason lies in the fact that both carbon steel and concrete have almost similar coefficients of thermal expansion; whereas, the thermal expansion coefficient of SS is about 80% higher than that of concrete [2, 3]. Thus, when the temperature of a reinforced concrete (RC) section increases, the thermal incompatibility between SS bars and concrete results in stresses that are not experienced by carbon steel RC sections.

At early age of concrete, heat is released from the exothermic hydration reaction, occurring between cement and water. The heat of hydration increases the temperature of the concrete mix and the embedded reinforcing bars. The temperature increase can reach 55°C in mixes with high cement content [4]. Ordinary Portland cement is composed mainly of aluminite (C3A), aluminoferrite (C4AF), belite (C2S) and alite (C3S) [5,6]. Hydration reaction produces

Calcium Silicate Hydrate (C-S-H) Gel and Ettringite, that increase the concrete strength. Wet or air curing preserves a satisfactory temperature for the concrete and improves concrete properties [5]. The variation of the heat of hydration with time is given in Fig. 2.6.

The coefficient of thermal expansion of concrete and carbon steel bars are $1.1 \times 10^{-5} \text{ }^\circ\text{C}^{-1}$ and $1.2 \times 10^{-5} \text{ }^\circ\text{C}^{-1}$, respectively [9]. These close values imply an excellent thermal compatibility between the two materials. However, the thermal expansion coefficient of SS bars can exceed $1.8 \times 10^{-5} \text{ }^\circ\text{C}^{-1}$ [9]. This relatively large divergence from the concrete thermal expansion raises concerns about the possibility of additional thermal stresses that may cause cracks. This scenario is expected to be most critical during the curing period, while concrete tensile strength is very low, and concrete temperature is increasing due to the heat produced during the hydration process.

This chapter aims at numerically investigating the influence of heat of hydration on stress distribution in SS RC sections considering the thermal incompatibility between the two materials. A finite element model is developed and validated to examine the temperature distribution and stresses developed in SS RC sections. Water and air curing regimes are considered in the analysis.

3.2. Material Models

3.2.1. Concrete

The variations of the concrete compressive strength (f_c) and tensile strength (f_t) with time are assumed to follow Fig. 3.1, where f_c' and f_t' are the 28-day compressive and tensile strength, respectively. The concrete constitutive relationship is assumed to follow the model proposed

by Jin [10] and is idealized using ANSYS multilinear model [11]. The concrete strain at peak stress and Poisson's ratio are assumed 0.002 and 0.30, respectively. Concrete failure is assumed, when its strain reaches the crushing strain for unconfined concrete ($\epsilon_{cu}=0.0035$) [3].

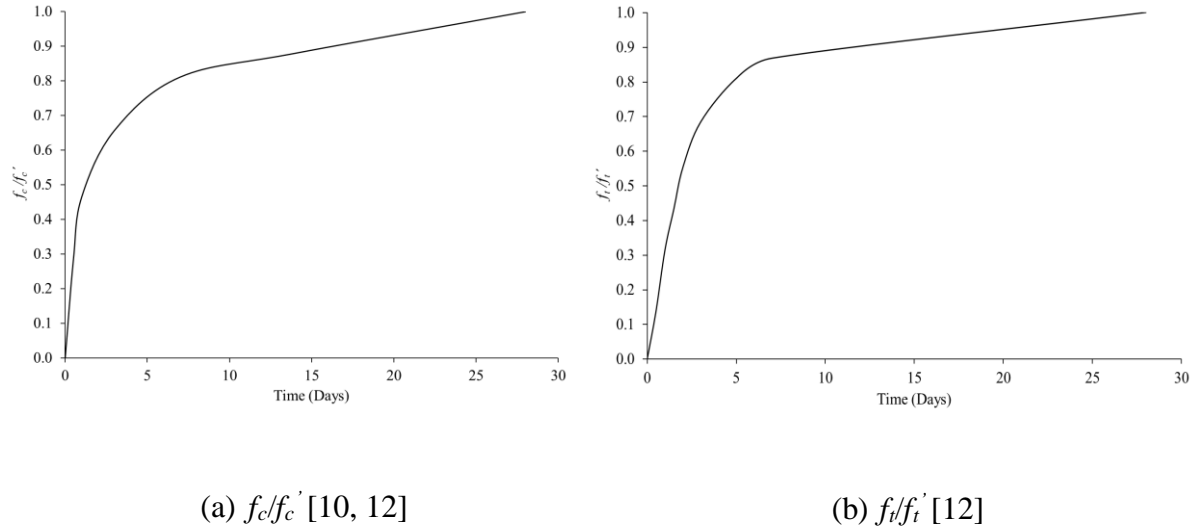


Figure 3.1: Variation of Concrete Strength with Time

The normalized compressive stress-strain relationship at various concrete ages is shown in Fig. 3.2. The figure shows that concrete compressive strength increases with time; whereas, its ductility decreases. The tensile behavior of concrete is predominantly brittle. Concrete is assumed to resist tensile stresses up to the cracking point beyond which the tensile capacity of concrete drops to zero.

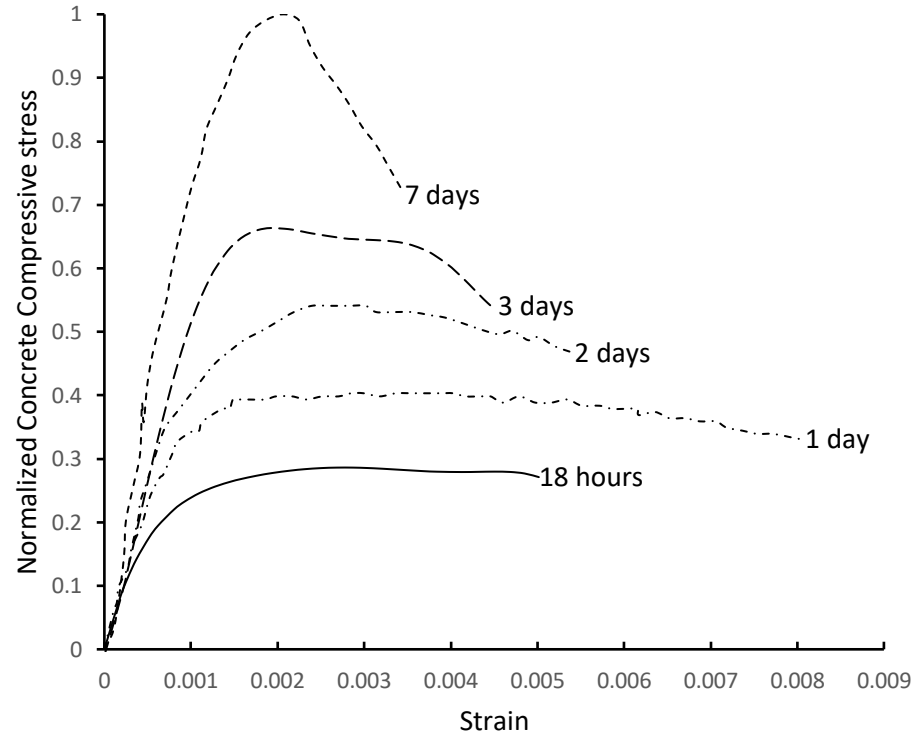


Figure 3.2: Stress-Strain Curves of Concrete at Early Age

The coefficient of thermal expansion of concrete, its specific heat, and its density are assumed $1 \times 10^{-5} \text{ } ^\circ\text{C}^{-1}$ [3], $920 \text{ J/kg}\cdot^\circ\text{C}$ [13] and 2300 kg/m^3 [14], respectively. The thermal conductivity of concrete is assumed to follow the values provided by EC2 [14] and shown in Fig. 3.3.

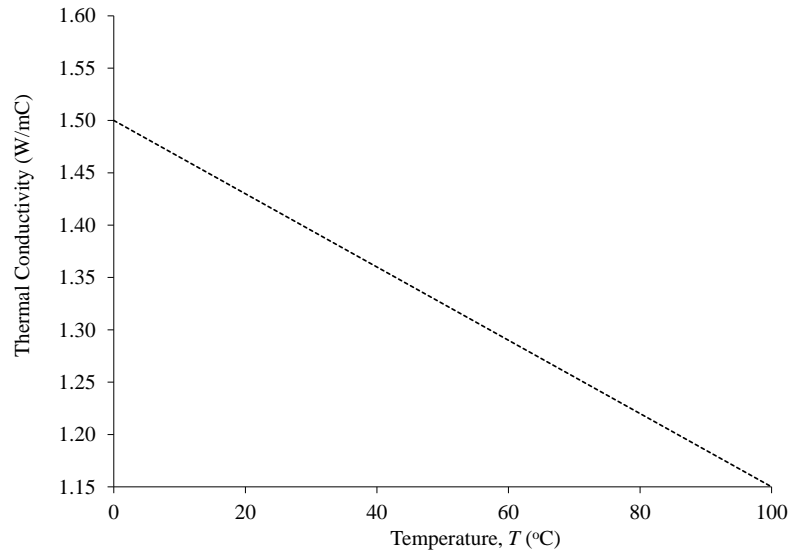


Figure 3.3: Thermal Conductivity for Concrete at Different Temperatures

3.2.2. Stainless Steel Bars

The constitutive relationship of SS bars is assumed based on the experimental work of Chen and Young [15]. The coefficients of thermal expansion of Austenitic 316LN and Duplex 2205 SS bars are assumed $1.8 \times 10^{-5} \text{ }^\circ\text{C}^{-1}$ and $1.3 \times 10^{-5} \text{ }^\circ\text{C}^{-1}$, respectively. The density, specific heat, and thermal conductivity of the bars are taken as 7750 kg/m^3 , $440 \text{ J/kg.}^\circ\text{C}$ [11] and $15 \text{ W/m.}^\circ\text{C}$ [16], respectively.

3.3. Finite Element Model

Fig. 3.4 shows a typical SS RC section considered in the analysis. The examined parameters are the section height (h), section width (b), concrete cover (c) and bar diameter (d). The section is assumed to be reinforced with two SS bars in tension and compression.

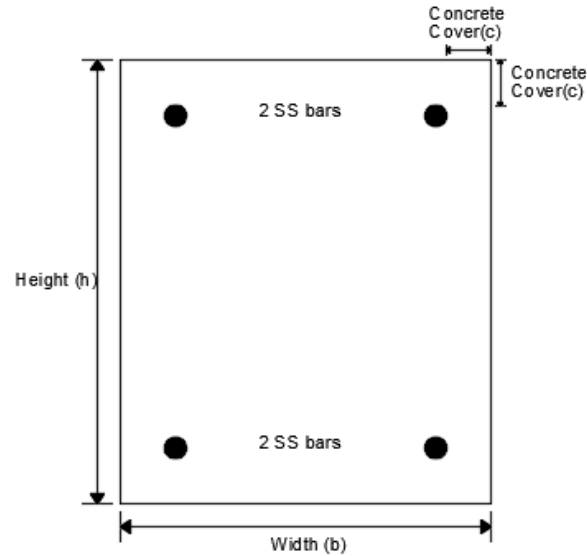


Figure 3.4: Typical SS RC Section

A two-dimensional thermal-structural analysis is performed using ANSYS 17.2 Finite Element Software [11]. Since the section is doubly symmetric in terms of geometry and applied temperatures, only the bottom left quarter is considered in the model. The analysis is performed by (1) selecting appropriate elements, (2) specifying thermal and structural material properties, (3) performing thermal analysis to determine the temperature due to heat of hydration at a specific time, and (4) performing a static structural analysis to determine the induced stresses and examine the potential for cracking.

3.3.1. Thermal Analysis

Both concrete and SS are modeled using PLANE77 [11], a two-dimensional 8-node thermal solid element. The element facilitates conducting two-dimensional steady-state analysis and is characterized of having temperature shape functions, which are well-suited to model curved geometries, such as the boundary between the concrete and the SS rebars. SURF151 and CONTA171 elements [11] are used at the boundary of the SS bar to model the interaction

between the SS rebar and the surrounding concrete. A typical meshed section is shown in Fig. 3.5. The optimum mesh density is chosen by performing a preliminary sensitivity analysis. A preliminary mesh, which is refined around the SS rebar, is first assumed. The mesh is then refined until the principal stresses have not exhibited significant variation, as compared to the subsequent refinements.

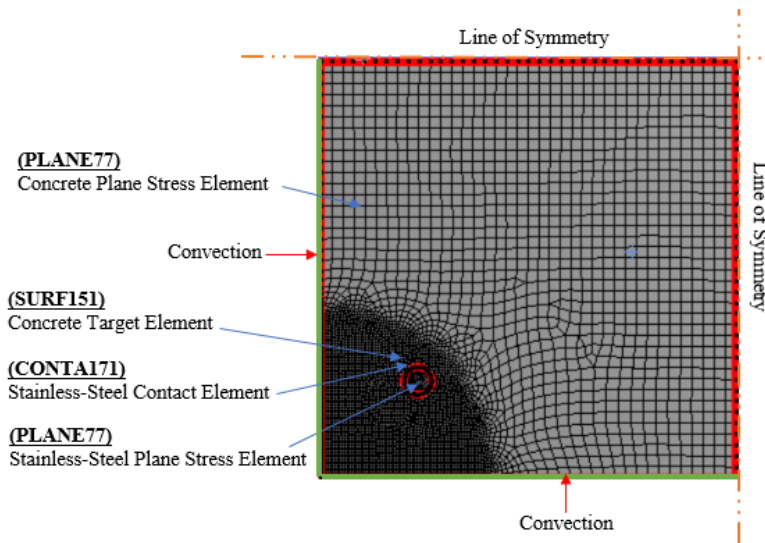


Figure 3.5: Thermal Analysis Mesh

RILEM Committee 42 [17] provided information about an experimental program that determined the relationship between the total heat liberated during the hydration reaction and time considering various water/cement ratios. For a water/cement ratio of 0.4, which ensures adequate amount of water to complete the hydration process, the relationship is shown in Fig. 3.6. The internal heat is generated by applying this relationship as a uniform internal energy that varies with time. Heat transferred by convection is applied on the exposed boundaries using convection coefficients of $12 \text{ kcal/m}^2\cdot\text{hr}\cdot^\circ\text{C}$ and $4.3 \text{ kcal/m}^2\cdot\text{hr}\cdot^\circ\text{C}$ for water and air curing, respectively [18, 19].

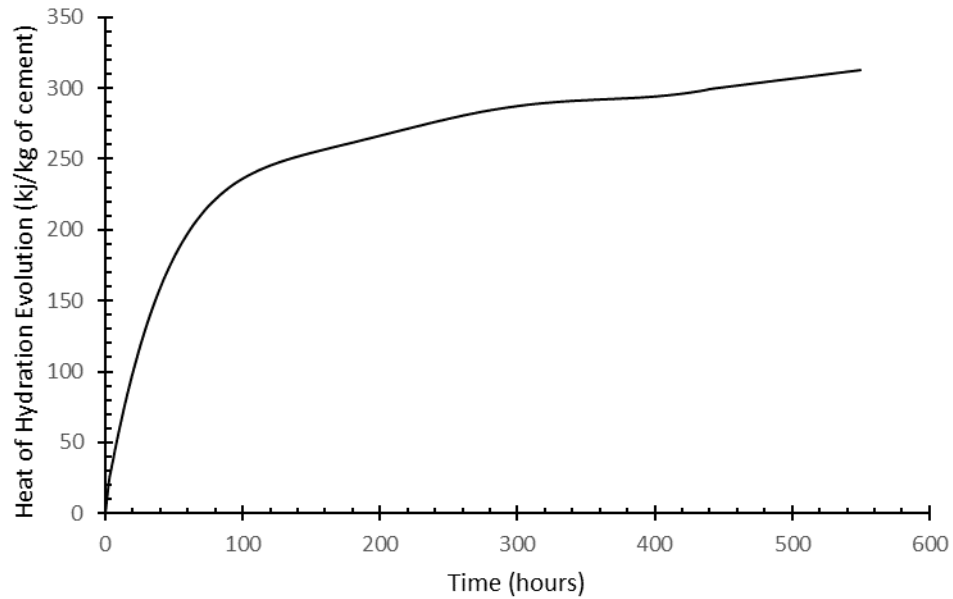


Figure 3.6: Heat of hydration at Different Ages [17, 20]

3.3.2. Structural Analysis Model

The thermal 2D element (PLANE77), used in thermal analysis, is replaced with an equivalent structural element (PLANE183) to model the concrete and SS rebars. This high order 8-node element provides quadratic displacement behavior with two translational degrees of freedom at each node. This feature allows the element to accurately capture the stress distribution. A typical structural mesh is illustrated in Fig. 3.7. The nodes along both lines of symmetry are restrained against orthogonal translational movement; whereas, the nodes along the free edges are unrestrained. The temperature values, reached in the thermal analysis stage, define the applied thermal loads.

The contact between concrete and the boundaries of the SS bars is simulated by CONTA172 [11] and the associated target element TARGE169 [11]. These elements can capture the

deformations of the boundaries. Concrete is considered as the target element, as it is expected to resist the SS rebar expansion.

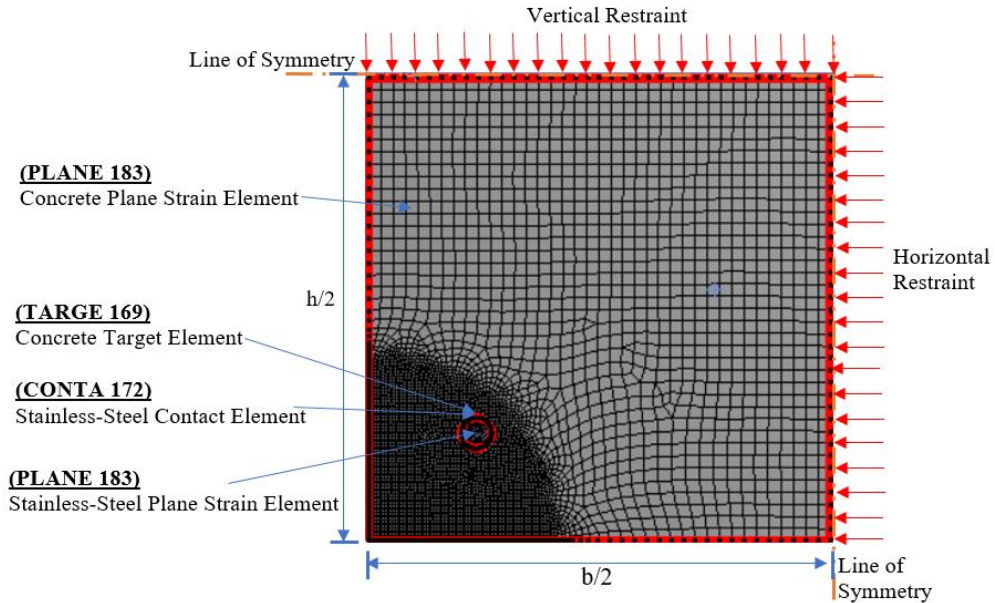


Figure 3.7: Structural Finite Element Model

3.4. Validation

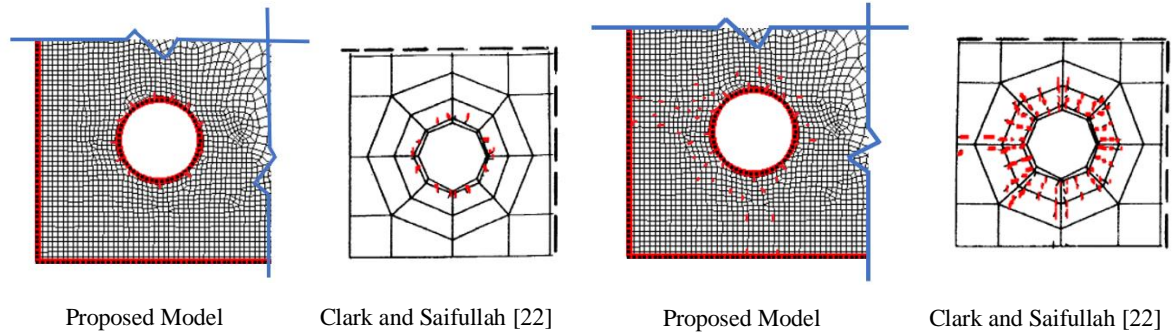
Unfortunately, the current literature lacks experimental data related to the effect of radial thermal expansion of SS bars on concrete at early age. However, Du et al. [21] conducted finite element analysis to determine the influence of corrosion-expansion of steel bars, on the structural response and cracking behavior of concrete elements. The results revealed the significant role of reinforcement radial expansion on crack formation. A finite element model was also developed and validated by Du et al. [21]. Clark and Saifullah [22] conducted accelerated corrosion tests to study the effects of corroded reinforcement on bond strength and concrete cracking.

Since the mechanism of stress development in the proposed research is similar to that of corroded bars, the results obtained by Clark and Saifullah [22] are considered to validate the finite element model. The RC section considered by Clark and Saifullah [22] had cross-sectional dimensions of $h = 175$ mm and $b = 150$ mm. A maximum mesh size of 3 mm was used to model the concrete. Reducing the size to 2.5 mm was found to alter the stresses by 0.2%, which was assumed negligible. The concrete is modeled with a void at the location of each corroded bar. The radial thermal expansion of the steel bars due to corrosion was simulated by applying radial displacement at the concrete nodes in the vicinity of the voids.

The obtained crack pattern is evaluated and compared to the data provided by Clark and Saifullah [22] as shown in Fig. 3.8. As the radial expansion of the corroded reinforcement increases, cracking of concrete has followed the same stages described by Clark and Saifullah [22]: (1) internal cracks, as shown in Fig. 3.8 (a), which have started at radial expansion of 0.00044 mm, as compared to 0.00050 mm by Clark and Saifullah [22], (2) external cracks, as shown in Fig. 3.8 (b), which have resulted in the formation of surface cracks at radial expansion of 0.00135 mm, as compared to 0.00120 mm by Clark and Saifullah [22], (3) penetration cracking, as shown in Fig. 3.8 (c), which have connected the surface cracks with the internal ones at radial expansion of 0.0016 mm, as compared to 0.0015 mm found by Clark and Saifullah [22], and (4) ultimate cracks, as shown in Fig. 3.8 (d), which includes all the potential cracks at radial expansion of 0.0019 mm, as compared to 0.0017 mm as found by Clark and Saifullah [22].

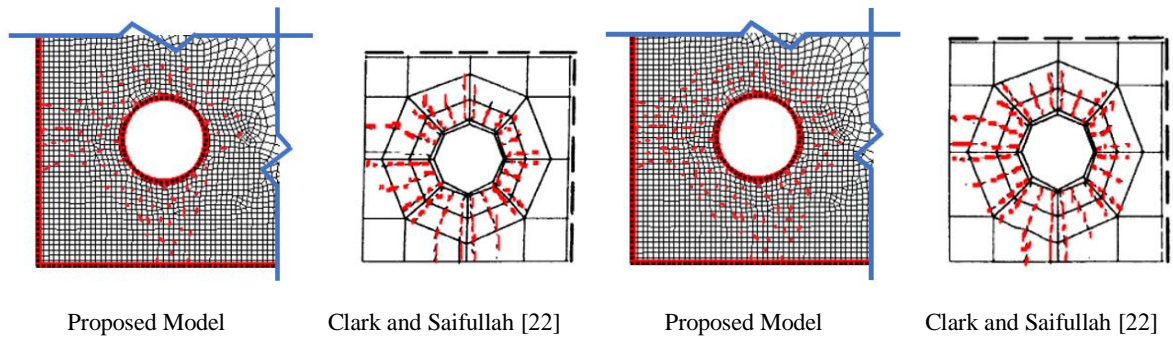
To further validate the model, the variation of radial expansion with the ratio of concrete cover to bar diameter (c/d) is determined and compared to the results obtained by Clark and Saifullah

[22], as illustrated in Fig. 3.9. The prediction error has ranged between 9% and 14%, which is considered acceptable given the complexity of the problem.



(a) Internal Cracks

(b) External Cracks



(c) Penetration Cracks

(d) Ultimate Cracks

Figure 3.8: Cracking of concrete due to radial expansion a cover equal to the bar diameter

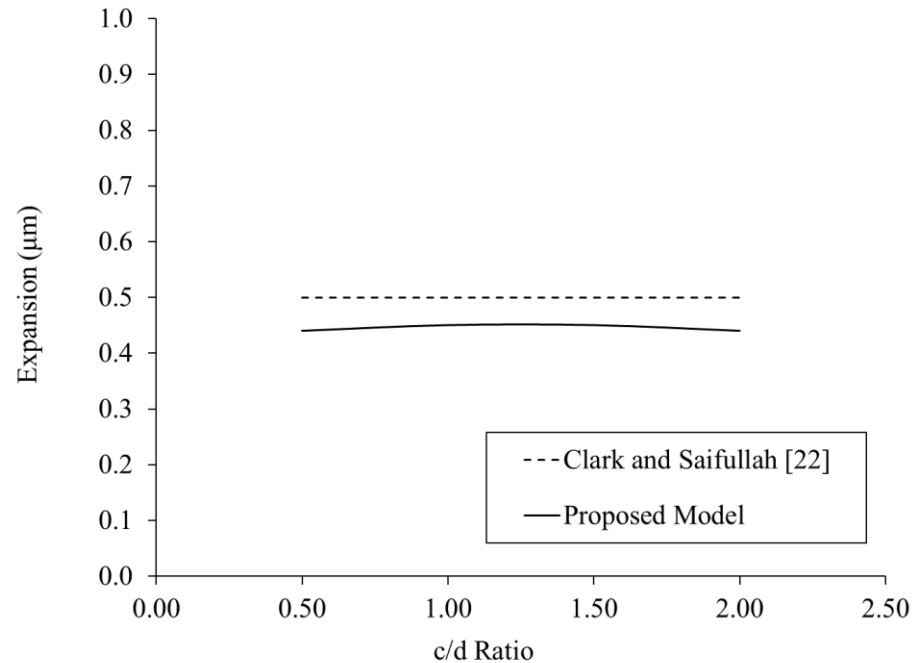


Figure 3.9: Radial Expansion at Cracking

3.5. Parametric Study

A parametric study is carried out to investigate the influence of varying the cross-section dimensions, bar diameter, SS type, and curing method on the radial thermal stresses developed in SS RC sections. Two sections, with dimensions of 300x300 mm and 600x600 mm, are considered in the analysis. Both 316LN and Duplex SS bars with diameters of 20 mm and 30 mm are examined. Both air curing and water curing are considered. Concrete cover, concrete tensile strength and concrete compressive strength are assumed as 35 mm, 3.8 MPa, and 30 MPa, respectively. Therefore, a total of 16 different cases are assessed.

The optimum mesh size is chosen based on a sensitivity analysis to vary between 0.85 mm for locations adjacent to the reinforcing bars and 4.0 mm at the core of the concrete section. Boundary conditions and the generated heat of hydration are applied, as discussed previously

in Section 3 of this chapter. Changing SS bar diameter is found to have negligible influence on the temperature distribution within the concrete section, resulting in a maximum difference of less than 1%. Also, varying the SS bar type did not have any effect on the temperature distribution as both 316LN and Duplex SS bars possess almost identical thermal properties.

The variation of temperature with time due to hydration reaction at a point located at the center of the considered RC sections is illustrated in Fig. 3.10 considering 20 mm SS bars (D20), sections with 300 or 600 mm dimensions (C300 or C600), and cooling using air or water (A or W). All curves follow the same general trend, which is characterized by a sharp increase in temperature during the initial period until reaching a peak value at about one day. After that, the temperature decreases gradually with a decreasing rate. For the same cross-sectional dimensions, air-cured specimens exhibit higher temperature values than their counterparts subjected to water-curing. This is caused by the higher convection coefficient for water, which affects the heat transfer at the interface between the concrete specimens and the surrounding medium.

The rising rate of temperature in the air-cured specimens is found to be about 50% higher than the water-cured specimens considering a width of 300 mm. By increasing the specimen's width to 600 mm, the change in rate drops to about 25%. This variation is attributed to the larger volume in the second case and consequently the further away the center of the section from the surface. Therefore, the internal points will be less affected by the variation of the curing regime as the dimensions of the concrete block increase.

Doubling the side length of the examined concrete sections from 300 mm to 600 mm resulted in increasing the initial rate of temperature from 15.3 °C/day to 30.3 °C/day for air cured specimens and from 7.8 °C/day to 22.8 °C/day for water-cured specimens. This change is

attributed to the higher amount of heat energy from the exothermic hydration reaction in larger specimens, as compared to the smaller ones.

After one day, the heat energy released from the hydration reaction decreases gradually. This results in reducing the temperature, as indicated in Fig. 3.10. In the 300 mm specimens, the reduction rate is almost identical for both air-curing or water-curing. However, by increasing the section dimensions to 600 mm, the reduction rate in the water-cured specimens becomes about 25% higher than that of the air-cured specimens. This is attributed to the larger distance from the section center to the surface and the higher heat energy generated in larger specimens.

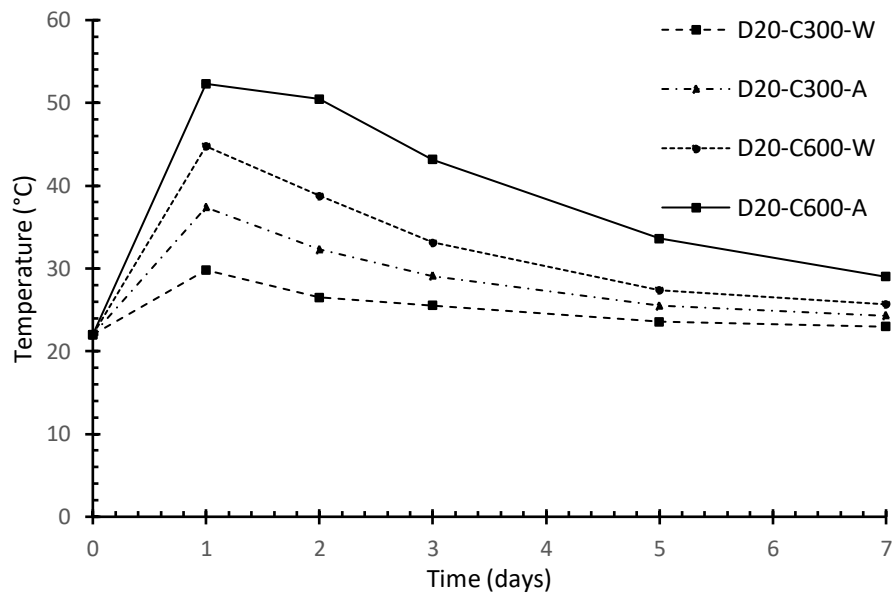


Figure 3.10: Variation of maximum Hydration Temperature with Time

Peak temperature distribution within D20-C600 specimen after one day is shown in Figs. 3.11(a) and 3.11(b) for water-curing and air-curing regimes, respectively. For both regimes, the temperature is maximum at the concrete center and its value decreases gradually until reaching the surface. At any point within the examined sections, temperature is lower in the water-cured

specimens than the air-cured specimen. This difference is more apparent in the outer elements that are located near the curing medium. The temperature of the embedded SS bar is assumed to be identical to that of the adjacent concrete elements.

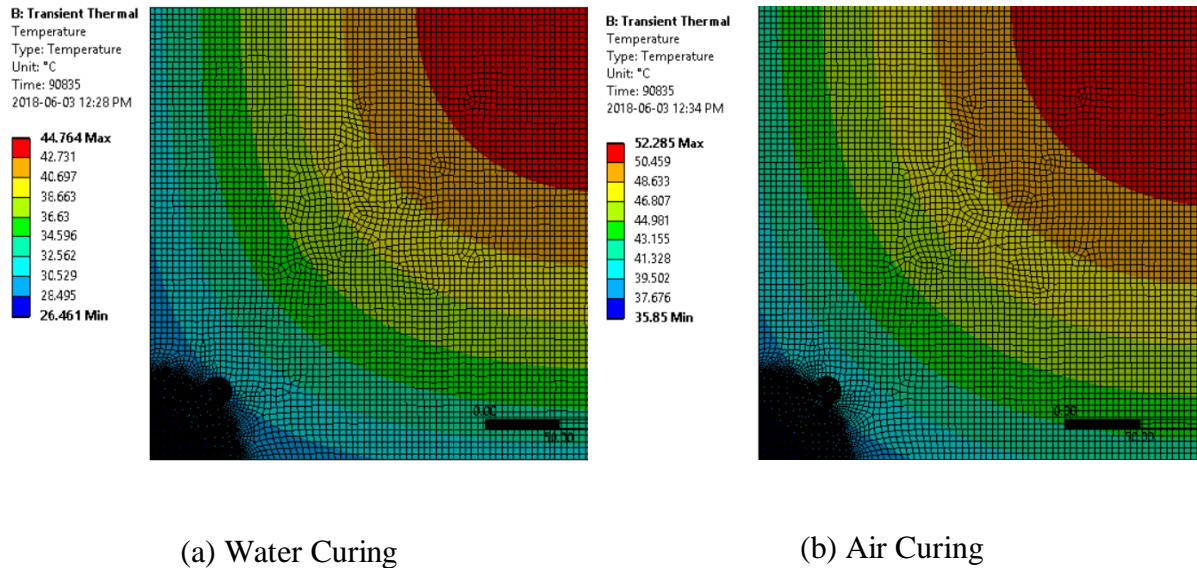
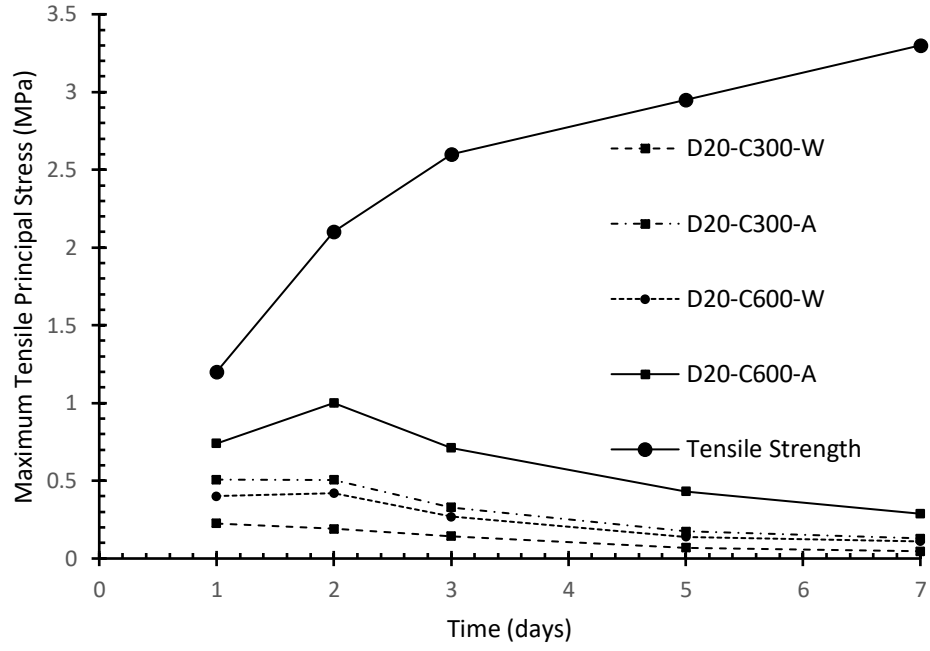
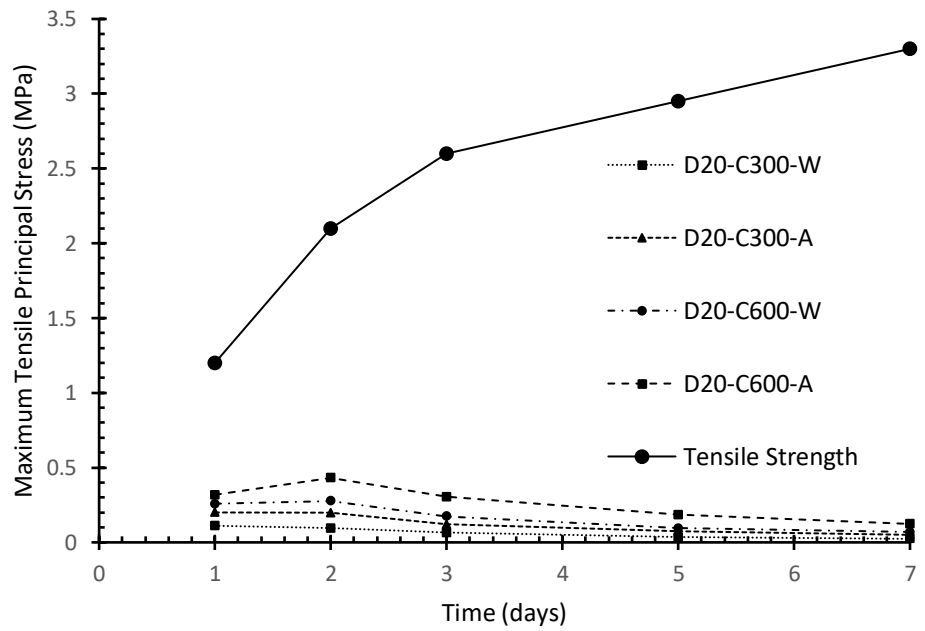


Figure 3.11: Temperature Variation after 1 Day for D20-C600

Figs. 3.12(a) and 3.12(b) illustrate the variation of the principal tensile stresses considering 316 LN and Duplex SS bars, respectively. The concrete tensile strength is also shown. The continuous increase in concrete tensile strength is attributed to the continuous hydration reaction, taking place at the early age of concrete. The principal tensile stress increases during the first day until reaching a peak, beyond which a gradual decrease is experienced over a longer duration. This behavior follows the trend of the temperature distribution resulting from hydration reaction. As the temperature increases, thermal expansion in the SS bars increases in a higher rate than the surrounding concrete causing higher thermal stresses to develop.



a) 316 LN



b) Duplex

Figure 3.12: Maximum Tensile Principal Stresses at Various Ages

Fig. 3.13 illustrates the principal stress distribution in Section D20-C300 after 1 day of hydration. The figure shows that the principal stress in concrete is maximum near the SS bars and decreases toward the surface. Changing the size of the SS bar from 20 to 30 mm had insignificant effect on the peak tensile stress since the temperature variation did not exceed 5%. Increasing the section cross section from 300 x 300 mm to 600 x 600 mm increased the developed stresses by an average of 55% around the SS bar. By changing the curing regime from water-curing to air-curing, a 150% increase in stress was observed in all sections reinforced with 316 LN SS bars. Considering Duplex reinforcement, the stresses increased by 100% for C300 sections and by 60% for C600 sections.

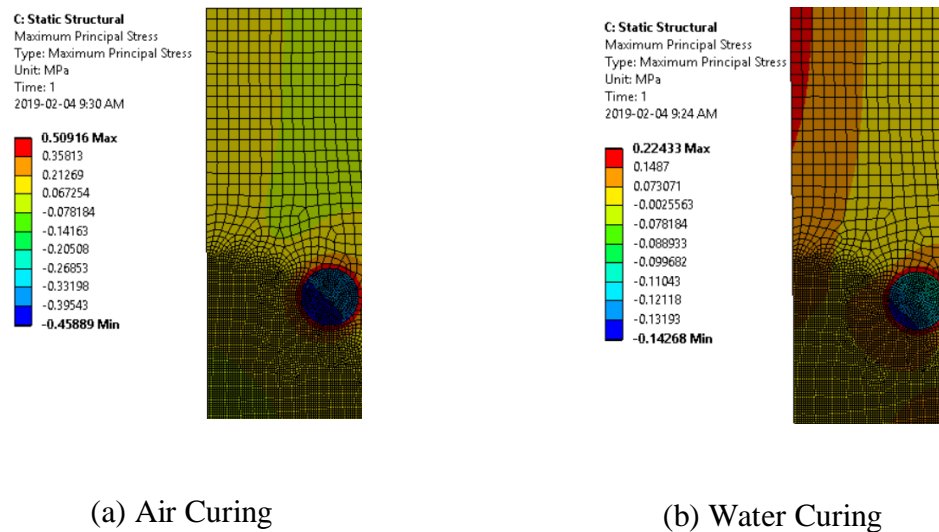
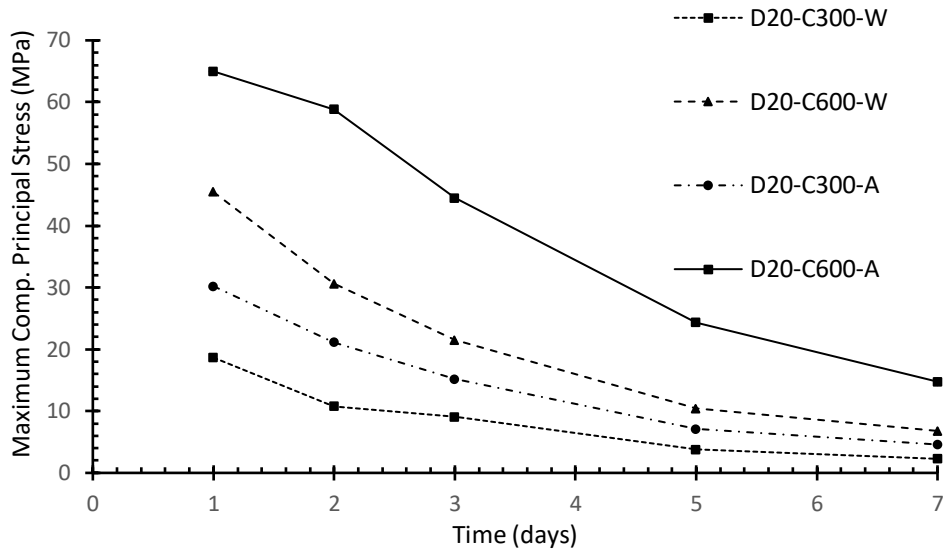


Figure 3.13: Tensile Stress Contours after 1 Day for D20-C300

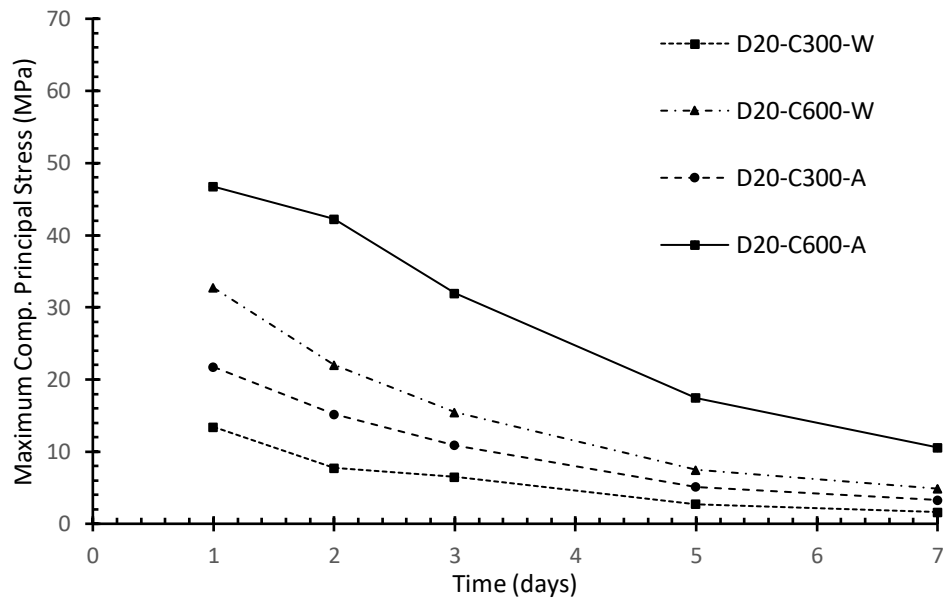
The variation of the maximum radial compressive stresses in the SS bars with concrete age is illustrated in Fig. 3.14. In all specimens, the peak stress is reached after one day of curing, when the temperature in the vicinity of the SS bar is the highest. After that, the heat generated from

the hydration reaction decreases with time leading to a continuous reduction of the peak stress until reaching a minimum value at the end of the examined period. Varying the size of the SS bars from 20 mm to 30 mm had a negligible influence on the maximum radial compressive stress developed in the bars. Doubling the dimensions of the square cross-section increased the stresses by about 50%. The curing method is found to have a significant influence on the induced stresses in the SS bar with time. For specimens with the same cross-sectional dimensions and bar size, water curing caused a reduction in the principal compression stress in the SS bar by about 65% and 40% compared to the air-cured specimens for Duplex and 316 LN bars, respectively.

Figs. 3.15(a) and 3.15(b) illustrate the variation of the radial thermal expansion of 316LN and Duplex SS bars at early age of concrete, respectively. The peak expansion is detected after one day due to the high activity of the hydration reaction and the excessive generation of heat energy. After that, a gradual decrease is noticed due to the reduction in the hydration rate. Increasing the diameter of the SS bars from 20 mm to 30 mm increased the radial expansion by about 35% and 65% in water-cured and air-cured specimens, respectively. Increasing the cross section from 300 x 300 mm to 600 x 600 mm raised the expansion by just under 50%. This is attributed to the higher temperature reached in the larger sections at the same concrete age. Changing the SS reinforcement from Duplex to 316 LN increased the expansion by 40% due to the difference in thermal coefficient between the two SS types.

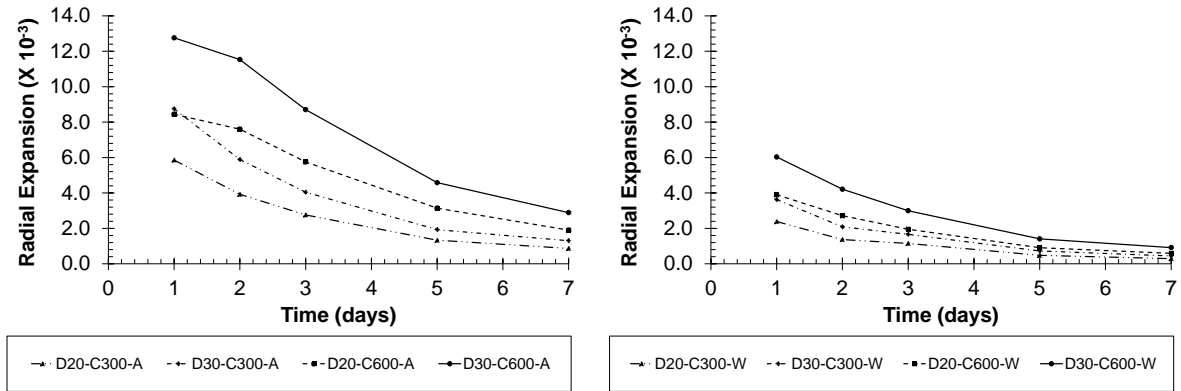


a) 316 LN



b) Duplex

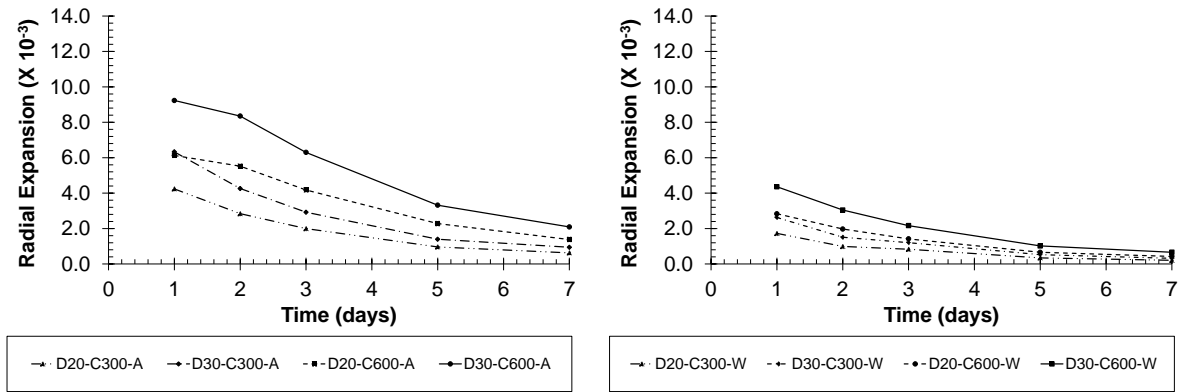
Figure 3.14: Maximum Compressive Principal Stresses at Various Ages



(i) Air Curing

(ii) Water Curing

(a) 316 LN



(i) Air Curing

(ii) Water Curing

(b) Duplex

Figure 3.15: Radial Thermal Expansion of SS bars at Different Ages

3.6. Summary and Conclusions

A thermal-structural finite element model was developed to analyze the behavior of stainless-steel reinforced concrete sections during the hydration process. First, a transient thermal analysis determined the temperature distribution within concrete. Then, a structural analysis determined the stress distribution inside concrete and stainless-steel radial expansion.

The variation in thermal expansion between concrete and SS results in the development of thermal stresses near the bars. Using Duplex SS bars minimizes these stresses and radial expansion of SS. Maximum Temperature inside concrete is affected by the size of the specimen. Radial thermal expansion of SS is affected by the temperature generated from the hydration reaction in the surrounding concrete and by the diameter of the SS bar. This expansion is restrained by the concrete matrix and generates thermal stresses in the vicinity of the steel bars. During the first two days, the concrete strength is relatively small whereas the generated stresses are at their peak. Therefore, minimizing the temperature is important to control the radial expansion of SS bars, especially within the first two days of casting the concrete. Continuous water curing of concrete reduces the principal stresses.

3.7. References

- [1] Meng, X.H. and Zhang, S.Y. 2016. Application and Development of Stainless Steel Reinforced Concrete Structure. MATEC Web of Conferences. 63, 03009. Wuhan, China
- [2] Canadian Institute of Steel Construction. 2016. Handbook of Steel Construction. Markham, Ontario. pp 7-47
- [3] CSA A23.3. 2014. Design of concrete structures. Cement Association of Canada, Ottawa, Ontario, Canada, 297 p.
- [4] Verbeck, G.J. 1968. Field and Laboratory Studies of the Sulfate Resistance of Concrete. Performance of Concrete, A Symposium in Honor of Thorbergur Thorvaldson, ACI and National Research Council of Canada, Reprinted as Portland Cement Association Bulletin RX227.
- [5] Kosmatka, S.H., Kerkhoff, B., and Panarese, W.C. 2002. Design and Control of Concrete Mixtures, fourteenth edition, Portland Cement Association, Illinois, p 47-49.
- [6] Zhi, G. 2005. Predicting Temperature and Strength Development of the Field Concrete, Ph.D. Dissertation, Iowa State University, Ames, Iowa, USA, 223 p.
- [7] Byfors, J. 1980. Plain Concrete at Early Ages. Swedish Cement and Concrete. Stockholm, Sweden, 464 p.
- [8] Mindess, S. Young, J.F. and Darwin, D. (2002). Concrete. 2nd Edition, Pearson Education, Inc, Upper Saddle River, New Jersey, USA. 644 p.
- [9] Nürnberger, U. 2005. Stainless steel reinforcement - a survey. Otto Graf Journal. 16:111-138.
- [10] Jin, X., Shen, Y. and Li, Z. 2005. Behaviour of High- and Normal-Strength Concrete at Early Ages. Magazine of Concrete Research, 57(6): 339-345
- [11] ANSYS User's Manual Release 12.0.1. 2009. Canonsburg, Pennsylvania, USA.

- [12] Kim, T. 2008. Concrete Maturity Method Using Variable Temperature Curing for Normal-Strength Concrete Mixes. *Journal of Materials in Civil Engineering*, 20(12): 735–741.
- [13] ACI Committee 207, Mass Concrete. *ACI Manual of Concrete Practice, Part 1*, 207.1, 1994. p. 18-24.
- [14] Background Documents to EN 1992-1-2 Eurocode 2: Design of concrete structures Part 1-2: General rules – Structural fire design, CEN, Brussels, Belgium
- [15] Chen and Young. 2006. Stress–strain curves for stainless steel at elevated temperatures. *Engineering Structures*. 28(2): 229 – 239.
- [16] Soudki, K.A, West, J.S, Campbell T.I, 2004. Effect of Temperature on Structural Performance of Stainless-Steel Reinforcement, MTO, Waterloo, Ontario, Canada, 82 p.
- [17] RILEM Committee 42. CEA, (1981), Properties of set concrete at early ages-State of-the-art report, RILEM, Vol. 14 – No 84, Paris, France.
- [18] Korea Concrete Institute. 2003. Standard Specification for Concrete. Korea Concrete Institute, Seoul, Korea.
- [19] Verbeck, G.J., and Foster, C.W., 1950, Long-Time Study of Cement Performance in Concrete: Chapter 6- The Heats of Hydration of the Cements, *Proceedings- American Society for Testing and Materials*, 50: 1235-1262.
- [20] ACI Committee 207, Effect of Restraint, Volume Change, and Reinforcement on Cracking of Mass Concrete. *ACI Materials Journal*, 87(3): 271-295
- [21] Du, Y., Chan, A. and Clark, L. 2006. Finite Element Analysis of the Effects of Radial Expansion of Corroded Reinforcement. *Computers and Structures*, 84: 917-929.
- [22] Clark, L.A. and Saifullah, M. 1993. Effect of Corrosion on Reinforcement Bond Strength. In: Forde M, editor. *Proceedings of 5th International Conference on Structural Faults and Repairs*, Engineering Technical Press, Edinburgh, UK, 3:113-119.

Chapter 4

4. PREDICTING THE FLEXURAL CAPACITY OF STAINLESS-STEEL REINFORCED CONCRETE SECTIONS CONSIDERING THE AXIAL LOAD LEVEL

4.1. Introduction

According to CSA A23.3-14 [1], analysis and design of flexural reinforced concrete (RC) members is performed based on the concept of stress-block parameters, which were proposed by Kazinczy [2] and Whitney [3]. In this approach, a fictitious rectangular stress block possessing the same resultant force and point of application with the actual compressive stress distribution is utilized. To satisfy the equilibrium conditions, the yield stress of the reinforcing bars should be known. However, in both Austenitic and Duplex stainless-steel bars, the point at which these bars yield is not well-defined [4]. Therefore, the procedure provided in the CSA A23.3-14 [1] cannot be implemented directly to calculate the flexural capacity of stainless-steel RC members.

This study aims at proposing a well-defined equivalent stress value that can be used to determine the flexural capacity of both Austenitic and Duplex stainless-steel RC members. To achieve this goal, the following objectives are considered and discussed in this chapter:

- 1- Conduct tensile tests on Austenitic and Duplex stainless-steel bars of different sizes to determine their actual stress-strain behavior.

- 2- Perform an experimental program to evaluate the structural performance of various stainless-steel RC beams and beam-column members under various configurations and loading conditions.
- 3- Create and validate a sectional analysis model in view of the results obtained from the experimental programs.
- 4- Utilize the validated analytical model to propose expressions for an equivalent stainless-steel stress value (f_{ss}) to calculate the flexural capacity of stainless-steel RC members following the procedure of CSA A23.3-14 [1].

4.2. Experimental Program

This section provides a description of the experimental program, which is performed in two phases. In the first stage, tensile tests are conducted on stainless steel bars to investigate their stress-strain behavior and to determine their actual constitutive relationship. The second stage aims at evaluating the structural performance of large-scale stainless-steel RC beams and columns.

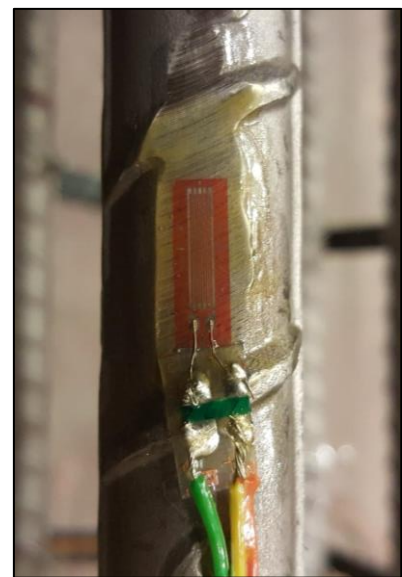
4.2.1. Tensile Tests on Stainless-Steel Bars

Axial tensile tests are performed on various sizes of both Austenitic and Duplex stainless-steel bars to determine their mechanical properties and deformation behavior. The bars are tested in the structural lab of Western University. The tensile tests are conducted in accordance with ASTM 370 [5] and with reference to ASTM A276 [6]. Three specimens of each size are tested until failure. Each specimen is subjected to monotonic tensile load using a universal testing machine in a displacement-controlled manner at a rate of 0.1 mm/min until the yielding region

is achieved, beyond which the strain rate increased to 2.2 mm/min until failure. The in-plane displacement is measured automatically by the movement of the machine head; whereas the strains at the central part of each bar is measured using a linear electrical resistance strain gauge mounted on the surface. The test setup and a close-up view of the strain gauge are shown in Figs. 4.1(a) and 4.1(b), respectively.



(a) Steel bar during testing



(b) Attached Strain gauge

Figure 4.1: Tensile test of the Stainless-Steel Bars

4.2.2. Large-Scale Tests Performed on Beams

An experimental program is performed to determine the load-deflection relationship of four large-scale stainless-steel RC beams. The cross-sectional dimensions of all beams are identical with a width of 250 mm and height of 400 mm. The total length of each simply-supported beam

is 2440 mm and the span between the supports is 2200 mm. The clear concrete cover is 35 mm. The type of the used stainless-steel bars and the reinforcement ratio vary between the beams as detailed in Table 4.1. The cross-sectional details of the tested beams are shown in Fig. 4.2.

Table 4.1: Description of the Beam Specimens

No.	Specimen Designation	Type of Main Steel Bars	Main Steel Bars	Secondary Steel Bars	Shear Reinforcement
1	B1	Duplex	3M20	2M10	10M@200 mm
2	B2	Austenitic	3M30	2M10	10M@200 mm
3	B3	Duplex	5M20	2M10	10M@200 mm
4	B4	Austenitic	5M30	2M10	10M@200 mm

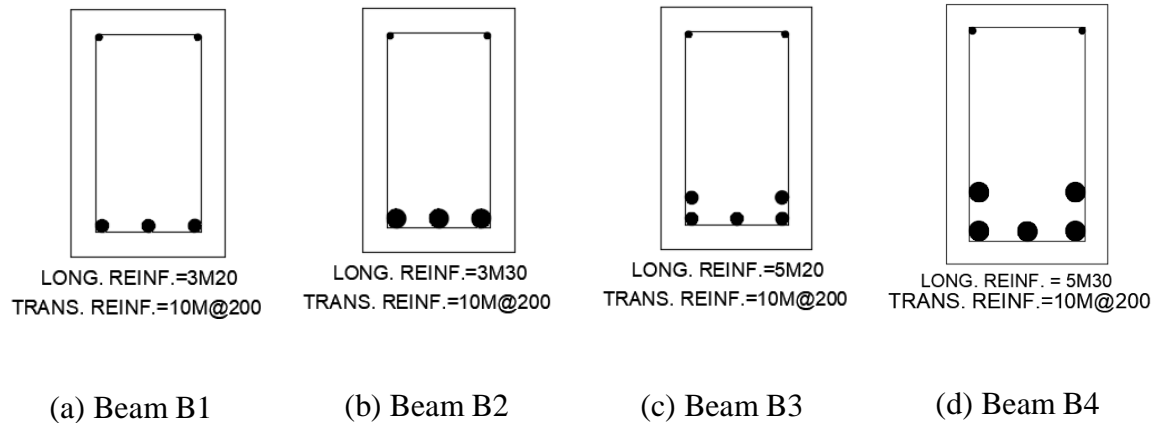


Figure 4.2: Cross-Sectional Details of the Tested Beams

Normal-strength Portland cement concrete is considered to construct the four large-scale beams. Seven standard concrete cylinders are tested after 28 days to evaluate the concrete strength in accordance with ASTM C39 [7]. The concrete compressive strength and modulus of rupture are found to be 37.0 MPa and 3.1 MPa, respectively. The concrete beams are tested after 28 days from construction. The steel cages are erected using stainless-steel bars as the main reinforcement and carbon steel as compression and vertical reinforcement as shown in

Fig. 4.3(a). A total of 4 strain gauges are mounted to the top and bottom longitudinal reinforcement of each beam to measure the variation of strains with the applied load at the mid-span section. Plywood panels are used to construct the formworks. Wood wedges are provided to protect the formwork from any lateral movement as shown in Figs. 4.3(b) and 4.3(c). A layer of grease is applied on the interior surface of the formwork to facilitate the removal of the concrete beam after hardening. Concrete is cured for 28 days by covering the formworks with moist burlap. After that, the beams are removed from the formwork and stored in the lab until testing.

The four beam specimens are tested in a one-point loading scheme as shown in Fig. 4.3(d). The load-deflection curve and deformation behavior are measured using linear variable displacement transducers (LVDT) at the soffit of the beams at their mid-span section. Load is applied to the specimens using a load-controlled hydraulic actuator at a rate of 20 kN/sec. The testing ends once crushing of concrete at the extreme compression fiber is observed.



(a) Steel Cages of the Considered Beams



(b) Steel Cages in Formworks



(c) Concrete Poured into Formworks



(d) Test Setup

Figure 4.3: Fabrication and Testing of the Beam Specimens.

4.2.3. Large-Scale Tests Performed on Columns

To further investigate the influence of stainless-steel bars on the structural performance of concrete members, a second phase of the experimental program is carried out by testing four large-scale stainless-steel RC columns. The examined columns have fixed cross-sectional dimensions of 300 mm x 300 mm and a total height of 2200 mm. A cantilever is constructed at the top end of each column to facilitate the application of an eccentric axial load. Another cantilever is constructed at the lower end of each column to provide a stable support for the columns during testing. The cantilevers are designed to ensure that they do not exhibit premature failure before reaching the full capacity of the columns. Both cantilevers have a depth of 700 mm and width of 300 mm. The eccentric loads are applied at distance of 400 mm from the centerline of each column. The type of the stainless-steel bars and the reinforcement ratio of the longitudinal steel bars vary between the columns as shown in Table 4.2. The cross-sectional details of the examined columns are shown in Fig. 4.4.

Table 4.2: Description of the Column Specimens

No.	Specimen Designation	Type of the Stainless-Steel Bars	Longitudinal Steel Bars	Column Ties
1	C1	Austenitic	12M20	10M@180 mm
2	C2	Duplex	12M20	10M@180 mm
3	C3	Austenitic	10M15	10M@180 mm
4	C4	Duplex	10M15	10M@180 mm

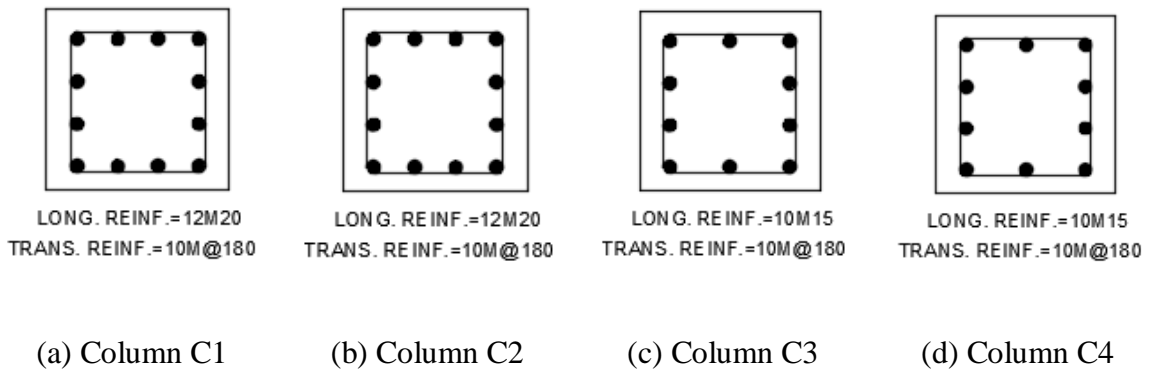


Figure 4.4: Cross-Sectional Details of the Tested Columns

The concrete columns are constructed from the same concrete mix used in the beams. A similar procedure is followed to fabricate the formworks and to erect the steel cages. The longitudinal reinforcement is made of stainless-steel bars; whereas the columns' ties and the cantilever's reinforcement are made of carbon steel. The formworks of the four column specimens before and after pouring the concrete are shown in Figs. 4.3(b) and 4.3(c), respectively. The erected steel cages are shown in Fig. 4.5. Four strain gauges are attached to the longitudinal bars at the mid-height of each column to obtain the strain profile along that section.



Figure 4.5: Steel Cages of the Tested Columns

The column specimens are subjected to eccentric concentrated loads at 400 mm from the centerline as illustrated in Fig. 4.6. Deflection at the mid-height of each column is obtained using an LVDT installed at the inner side of the columns. Monotonic incremental load is applied to the columns through a load-controlled hydraulic actuator at a loading rate of 20 kN/sec. The testing terminates once crushing of concrete is detected at the inner face of the column, where the compressive stresses are maximum.

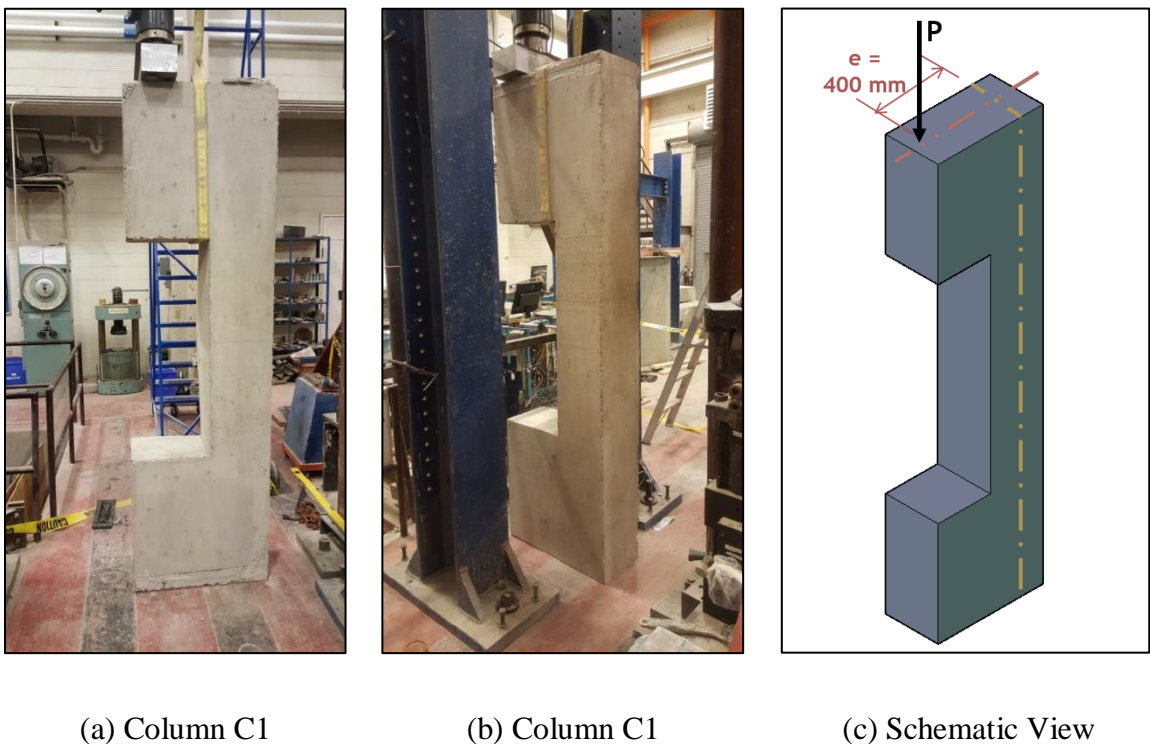


Figure 4.6: Test Setup for the SS Columns

4.3. Discussion of the Experimental Results

This section describes the test results obtained from the experimental program. The axial tensile tests conducted on the stainless-steel bars are used to evaluate the influence of varying the bar size and its type on the stress-strain relationship. The tests performed on the large-scale beams

and columns are used to evaluate the deformation behavior and characteristics of such members when stainless-steel bars are used as a reinforcing material.

4.3.1. Tensile Tests on Stainless-Steel Bars

The stress-strain curves are observed and recorded in the first phase of the experimental program. Three stress-strain curves of each bar type and size are obtained and a representative curve is plotted as shown in Figs. 4.7(a) and 4.7(b) for Austenitic and Duplex stainless-steel bars, respectively. The variation in the measured stress-strain relationship between the three curves is not significant. The mechanical properties, yielding region and ductility of each bar are determined from the reported stress-strain curves.

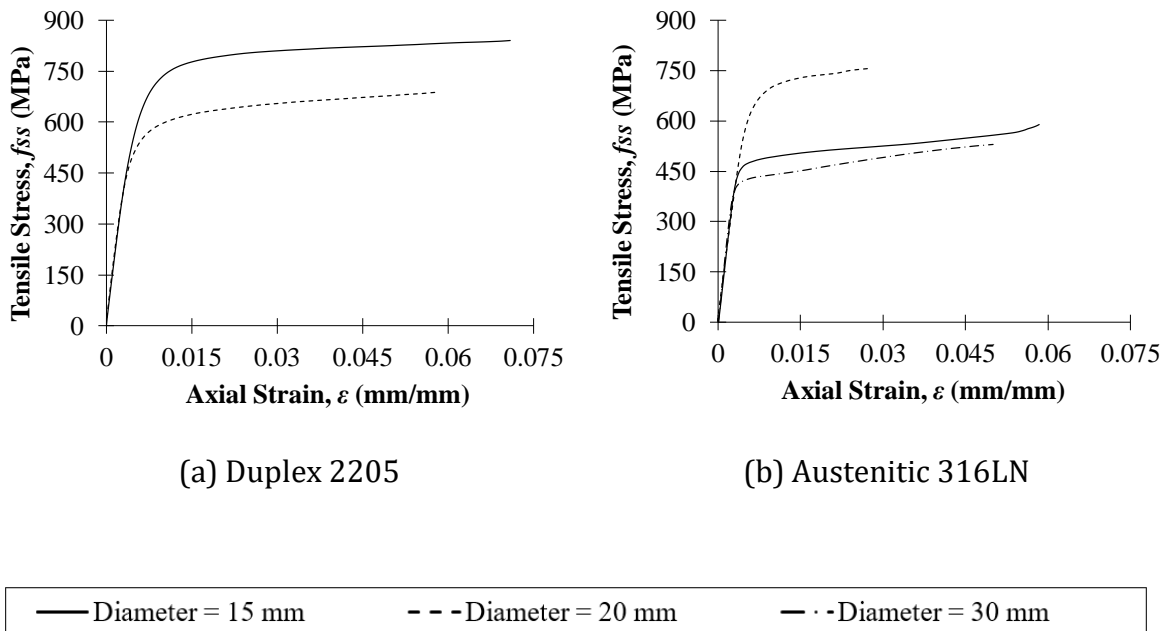


Figure 4.7: Stress-Strain Curves of the Experimentally Tested Stainless Steel Bars

The yield region of Duplex stainless-steel bars is higher than their Austenitic counterparts for the same bar size due to the microstructure variation between the two types [4]. The stress value within the yielding region is about 55% and 33.0% higher in the Duplex bars for diameters 15 mm and 20 mm, respectively. The observed difference between the stress-strain curves for different bar diameters is due to the fact that each bar diameter came from a different manufacturing patch. The modulus of elasticity of Duplex stainless-steel bars is 200 GPa, which is slightly higher than the 190 GPa obtained for the Austenitic bars. Failure of all specimens is governed by necking followed by fracture within the gauge length away from the machine grips. All bars experienced a ductile mode of failure as indicated by the significant deformation prior to fracture.

Mathematical expressions are proposed based on least squares regression to describe the stress-strain curves of all bars. The proposed expressions are shown in Appendix A for both type of bars.

4.3.2. Large-Scale Tests Performed on Beams

The structural performance of stainless-steel RC beams is evaluated based on the results obtained from the second phase of the experimental program. The assessment criteria include the load-deflection behavior, flexural capacity, ductility and failure mode. The influence of varying the reinforcement ratio and bar type on the capacity and deformation behavior is examined. The failure mechanism is investigated by observing the cracking pattern at various loads.

4.3.2.1. Load-Deflection Behavior

The load-deflection curves at mid-span section for the tested beams are shown in Fig. 4.8. The overall trend of beams B2 through B4 is identical and consists of a linear elastic region followed by a gradual decrease in the slope until failure occurs. The curves terminated at the peak point since the load is applied in a load-controlled manner. The deformation behavior of the beams shows a similar trend to the stress-strain curves of the embedded stainless-steel bars, which lack a well-defined yield plateau. Regarding beam B1, the curve shows abrupt changes at different locations due to technical issues related to the installation of the LVDT. However, the maximum applied load and the corresponding deflection are correctly measured.

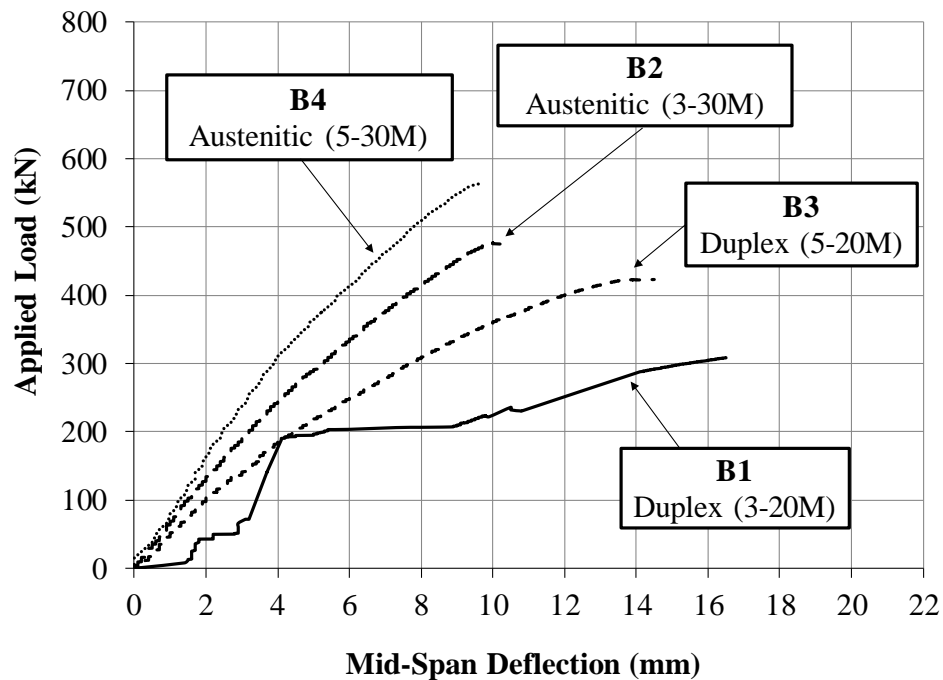


Figure 4.8: Load-Deflection Curves of the Tested Beams

The influence of varying the stainless-steel type and reinforcement ratio on the load-deflection relationship of the tested beams are investigated in view of Fig. 4.8. The one-point load is applied at the mid-span section and the corresponding deflection is measured at the soffit of

the beam at the same section. Beams B1 and B3 are constructed using 20M Duplex stainless-steel bars with a reinforcement ratio of 1.0% and 1.7%, respectively. On the other hand, beams B2 and B4 are constructed using 30M Austenitic stainless-steel bars with a reinforcement ratio of 2.5% and 4.1%, respectively.

A comparison between beams B2 and B4 shows that increasing the reinforcement ratio of the Austenitic stainless-steel bars from 2.5% to 4.1% does not affect their deformation behavior and failure mode. However, this increase has a significant influence on both stiffness and ultimate capacity of the examined beams. For instance, increasing the number of bars from 3-30M to 5-30M results in increasing the secant stiffness at 3 mm by about 25%. Similarly, the addition of the two extra bars increases the capacity by about 18.5% from 475 kN to just over 563 kN. The maximum deflection corresponding to crushing of the extreme compression fibers shows a small reduction of about 4.0% by increasing the number of bars. Flexural cracks in both beams are observed to initiate from the mid-span and propagate towards the supports. As the load increases, the cracks widen and continue upward toward the neutral axis until crushing of concrete occurs. A photo taken for beam B2 at the end of the test is shown in Fig. 4.9. The actual cracking pattern and failure mode are depicted in Figs. 4.10 (a) through 4.10 (d) for clarification.

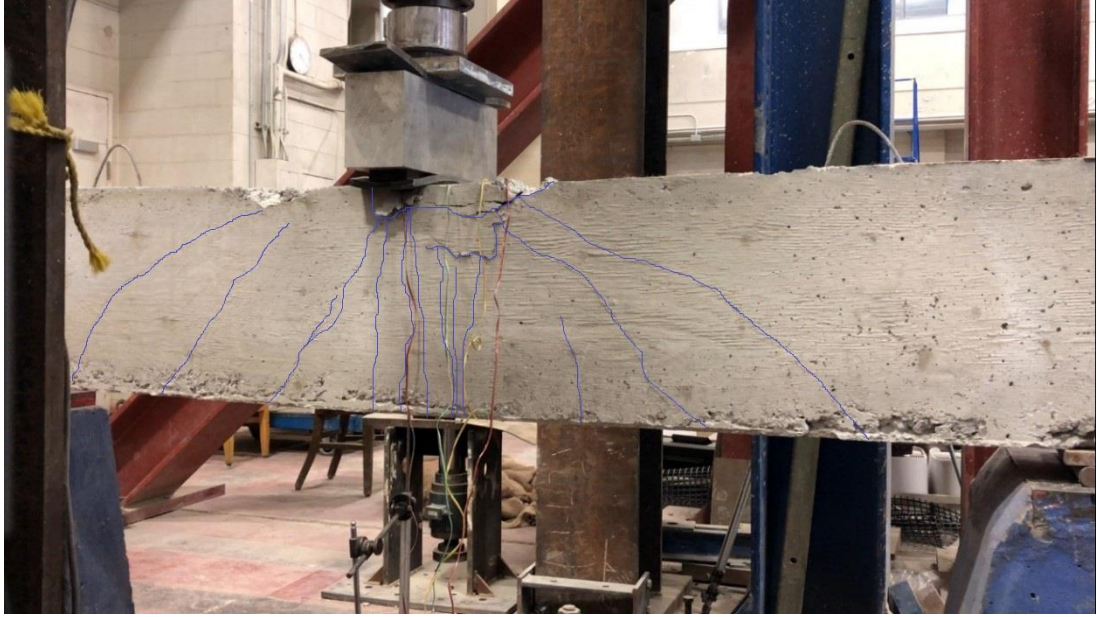
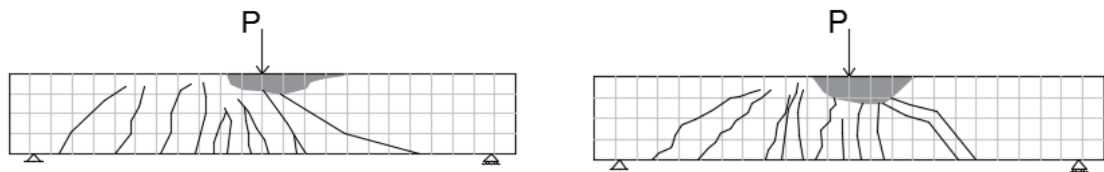
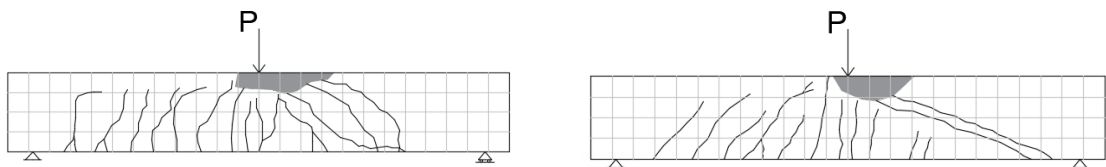


Figure 4.9: Typical Failure Mode of the Tested Beams



(a) Beam B1

(b) Beam B2



(c) Beam B3

(d) Beam B4

Figure 4.10: Cracking Pattern of the Tested Beams at Failure

For beams B1 and B3, Duplex stainless-steel bars are used as the main reinforcement. The deformation behavior of both beams follows the same trend as beams B2 and B4.

The test results show that increasing the reinforcement ratio from 1.0% to 1.7% results in an increase of about 37.0% in the flexural capacity as shown in Fig. 4.8. Increasing the number of bars from 3-M20 to 5-M20 results in a reduction of the ductility at the ultimate load by about 14%. This means that by increasing the reinforcement ratio of the stainless-steel RC beams, their ultimate capacity increases, and their ultimate deformation decreases. Thus, in general, as the flexural capacity of the stainless-steel RC members increases, their ductility decreases, and vice versa. The same observation is detected for conventional RC members [8]. The observed failure mode of Austenitic and Duplex stainless-steel RC beams is similar. Cracks initiate at the mid-span section and continue to form at different locations toward the supports. The cracks also widen and propagate upward as the load increases until concrete crushing is reached.

4.3.2.2. Strain Profiles

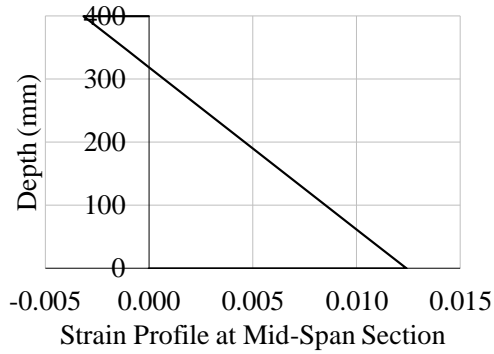
To further investigate the flexural performance of the beam specimens, the strain variation at the top and bottom steel bars is measured and recorded. At each side, two strain gauges are mounted on the opposite steel bars to ensure accuracy of the measurements. In all cases, minor deviations are detected between the opposing strain gauges.

The strain profiles at the mid-span section of beams B1 through B4 at ultimate capacity are depicted in Figs. 4.11(a) through (d), respectively. These profiles are plotted with the knowledge of the strain values at the upper and lower steel bars. The line connecting the two strain values assumes that plane sections remain plane after deformation. In general, the flexural capacity of the tested beams is reached when the strain at the extreme compression

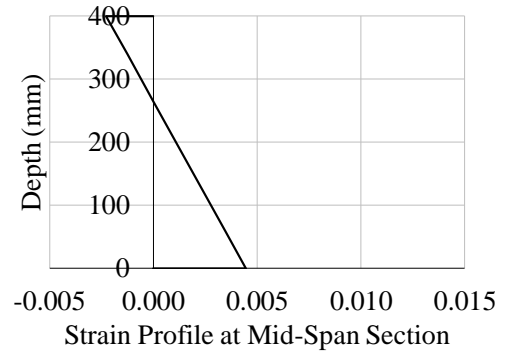
fiber is within the range 0.0030 to 0.0035. The corresponding strains Duplex and Austenitic stainless-steel bars have shown differences due to the higher reinforcement ratio used in the Austenitic stainless-steel RC beams. For instance, the strains at the bottom bars corresponding to ultimate capacity are 0.0103 and 0.0062 for beams B1 and B3, respectively. In beams B2 and B4, the strains at the bottom bars drop to 0.00344 and 0.0026, respectively. The higher strain values for Duplex stainless-steel RC sections explain the larger ultimate deflections in Beams B1 and B3 as compared to beams B2 and B4, as illustrated in Fig. 4.8.

In all beam specimens, increasing the reinforcement ratio results in a reduction of ductility as reflected by the maximum strain of the bottom steel bars. For example, increasing the number of bars from 3-20M to 5-20M in Duplex stainless-steel RC beams causes the strains in the main reinforcement to drop by about 40.0% from 0.0103 to 0.0062. Similarly, increasing the number of bars from 3-30M to 5-30M in Austenitic stainless-steel RC beams results in reducing the measured strain from 0.00344 to 0.0026, which represents a drop of approximately 25.0%.

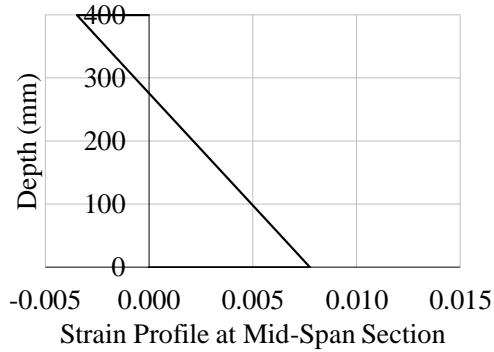
The variation of strains with load at the mid-span section is recorded at the top and bottom reinforcing bars. It is worth mentioning that two strain gauges are mounted at each side of the beam to ensure accuracy of the readings and to detect any twisting or irregular deformation in the beam. In all beams, the strain gauges, installed at the same level, show almost identical readings indicating that the observed readings accurately represent the flexural behavior of the beams.



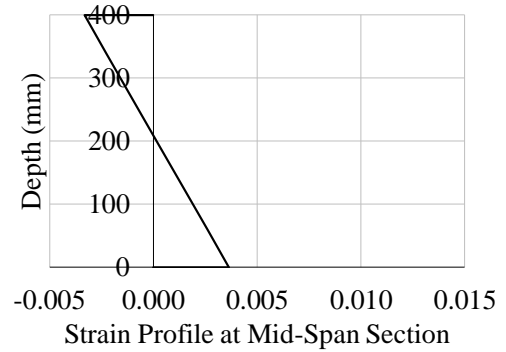
(a) Beam B1



(b) Beam B2



(c) Beam B3



(d) Beam B4

Figure 4.11: Strain Profile at Mid-Span Section of the Tested Beams

Fig. 4.12 shows the load-strain curves of two strain gauges placed at the top and bottom reinforcing bars in beam B4 at the mid-span section. The load-strain curve of the bottom reinforcement is linear up to 100 kN, beyond which the slope decreases until yielding followed by concrete crushing are observed. The reduction in slope is attributed to the propagation of flexural cracks along the soffit of the beam as the applied load increases. The deformation behavior for beam B4, shown in Fig. 4.8, has a similar trend to the slope of the load-strain curve

of the main reinforcement. The yielding stage is reached at a strain value of about 0.0021 beyond which the slope decreases suddenly indicating reaching the yielding stage.

The strain variation at the top reinforcement starts with a linear behavior until reaching approximately 40% of the maximum load value. After that, the slope decreases gradually until failure occurs. The curve has a similar behavior as the concrete compressive stress-strain curve. The maximum strain in the top steel bars, at which crushing occurs, is about 0.0021. Considering the strain profile at failure, the strain at the extreme compression fiber is determined to be 0.0033, as shown in Fig. 4.11(d).

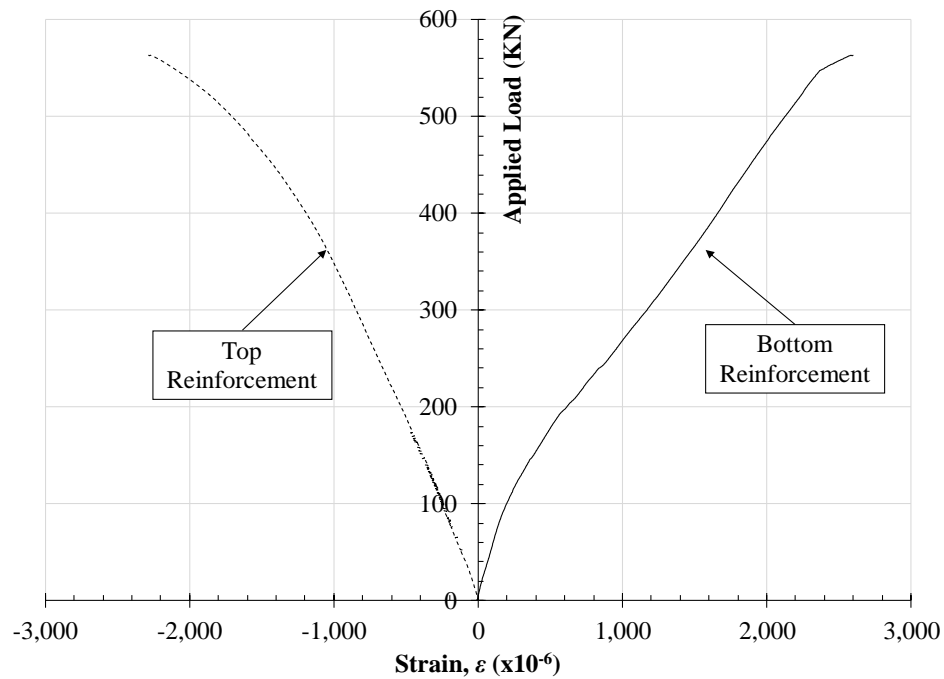


Figure 4.12: Strain Variation with Load at Mid-Span Section of Beam B4

4.3.3. Large-Scale Tests Performed on Columns

The structural performance of stainless-steel RC columns is evaluated in view of the experimental program conducted on the four large-scale columns. The behavior is evaluated based on the failure mode, strain distribution and load-deflection relationship of the eccentrically loaded columns. The investigated parameters are the reinforcement ratio and the type of the longitudinal stainless-steel bars. Cracking pattern and deformation behavior are observed and compared to the measured load-deflection curves and strain profiles.

4.3.3.1. Load-Deflection Behavior

The load-deflection curves at mid-height of the four examined columns are illustrated in Fig. 4.13. The general behavior of the tested columns is identical except for column C3, which encountered some technical issues in setting the LVDT. However, the first portion of the curve and the ultimate capacity are correctly measured. The LVDT is attached to the outer face of each column at the mid-height section to continuously measure the lateral deflection corresponding to the applied load.

Each curve is divided into three regions. In the first region, the concrete is uncracked, and the load-deflection curve increases in a constant rate until reaching a point, where the slope increases. This point defines the cracking load for the extreme tension fibers at the connection between the column and the cantilever. The higher slope indicates that for the same incremental increase in the applied load, the column deflects in a smaller rate than that observed in the first region. The increase in slope is attributed to the initiation and propagation of tension cracks. The third region is characterized by a gradual decrease in slope until failure occurs. The

reduction in slope is attributed to yielding of the outer longitudinal bars subjected to tension. Since the tests are carried out in a load-controlled system, failure is defined at the point of maximum applied load as shown in Fig. 4.13.

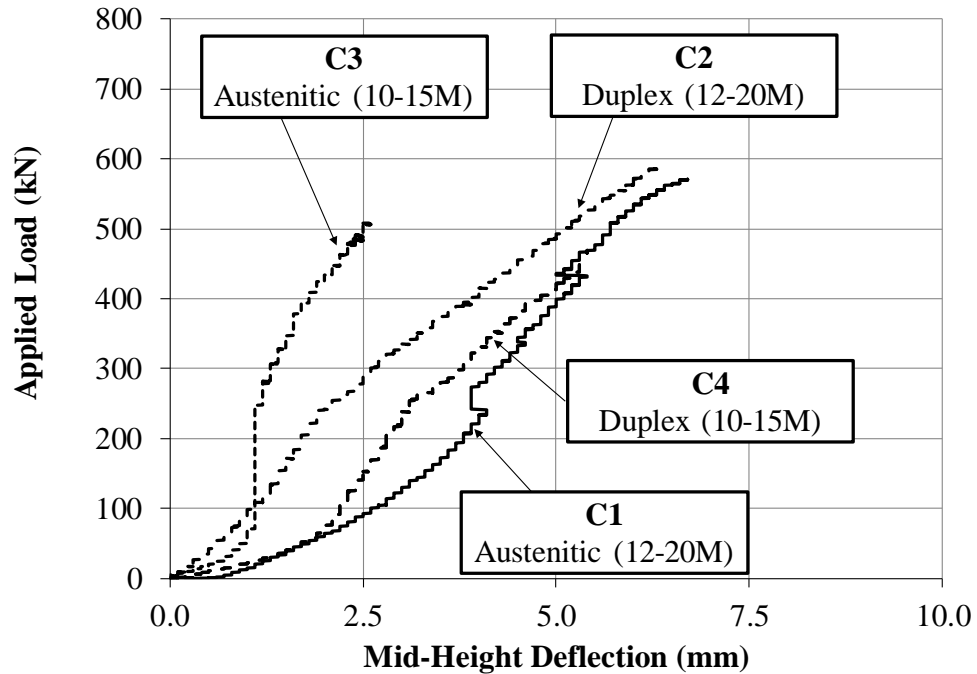


Figure 4.13: Load-Deflection Curves of the Tested Columns.

The effect of changing the type and number of longitudinal bars on the capacity and deformation behavior of the examined columns is considered. A concentrated load is applied at the end of the cantilever and the corresponding deflection is measured at the outer face of the mid-height section of the columns. Columns C1 and C3 are constructed using 12-20M and 10-15M Austenitic stainless-steel bars with a reinforcement ratio of 4.0% and 2.22%, respectively. Columns C2 and C4 are constructed of 12-30M and 10-15M Duplex stainless-

steel bars with the same reinforcement ratios. The failure of all column is detected at an axial load level of 0.14 except for column C4, which failed at a load level of 0.12.

Stiffness and capacity at which failure takes place vary depending on the reinforcing bars and their type. For instance, a comparison between columns C1 and C3 reveals that increasing the reinforcement ratio of the Austenitic stainless-steel bars from 2.22% to 4.0% results in increasing the capacity by about 11.5% from 512.3 kN to 571.1 kN. The observed deformation behavior and failure pattern of columns C1 and C3 are similar. This is indicated by propagation of tension cracks at the outer face of the column near the cantilever followed by concrete crushing at the interior face of the columns at the soffit of the cantilever. A representative photo taken for column C1 at the end of the test is shown in Fig. 4.14. The cracking pattern at failure of all columns is mapped to scale and depicted in Fig. 4.15. By examining the cracking patterns of columns C1 and C3, a ductile behavior can be detected.



Figure 4.14: Typical Failure Mode of Column C1

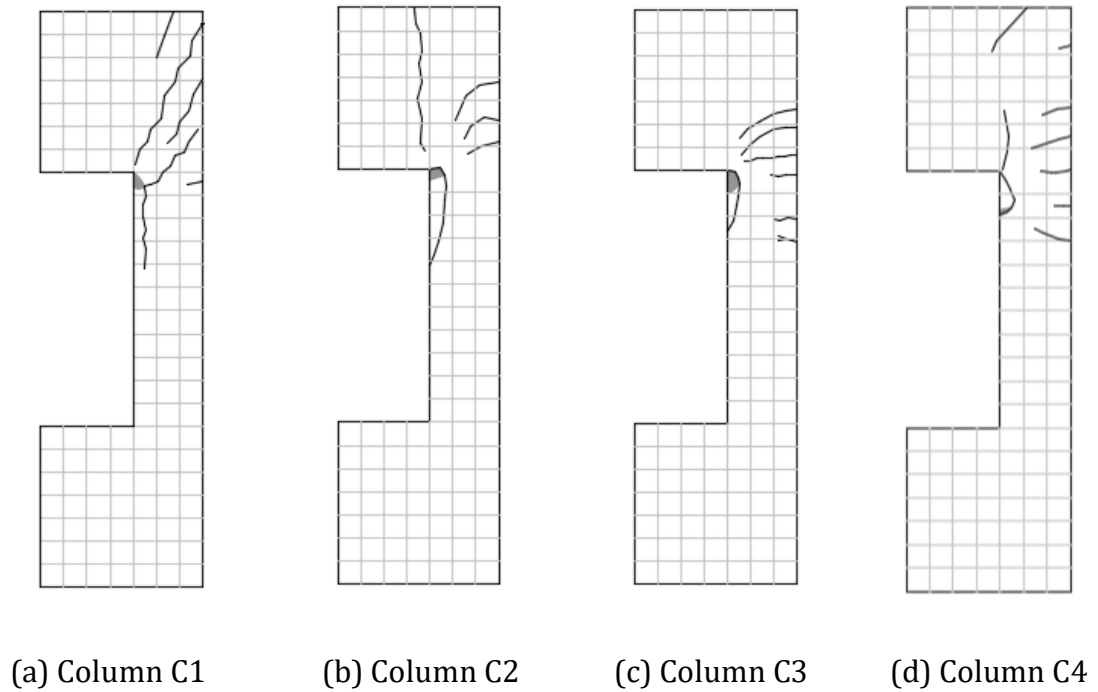
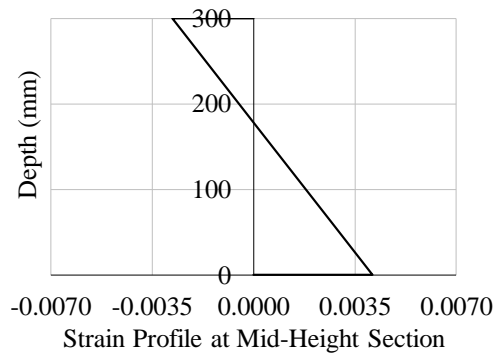


Figure 4.15: Cracking Pattern of the Tested Columns at Failure

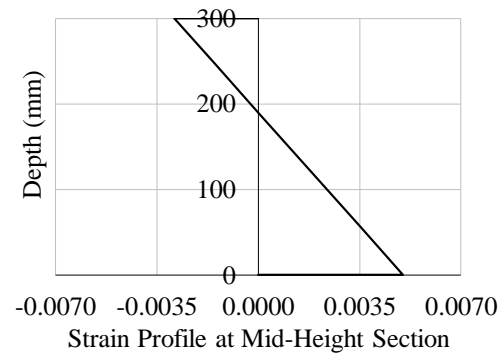
As for columns C2 and C4, Duplex stainless-steel bars are used as the longitudinal reinforcement. The deformation behavior observed for these columns is generally similar to that detected for columns C1 and C3. The test results show that increasing the reinforcement ratio from 2.22% to 4.0% results in an increase in ultimate capacity of about 34.0% from 437.7 kN to 586.1 kN. This change also results in decreasing the ductility, as reflected by the maximum deflection, by about 17.5% as shown in Fig. 4.13. This observation further confirms the findings obtained for beams showing that there is an inverse relationship between member's strength and its ductility in stainless-steel RC members. The failure mode of columns C2 and C4 is ductile and follows the same cracking pattern as columns C1 and C3. The cracking pattern at failure is illustrated in Figs. 4.15(b) and 4.15(d) for columns C2 and C4, respectively.

4.3.3.2. Strain Profiles

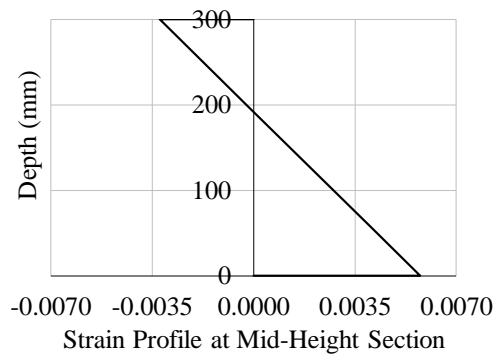
Strain variation is measured and recorded by installing strain gauges on the longitudinal bars at the mid-height section of the examined columns. Two strain gauges at each side are attached to the opposite bars to verify the measurements and to detect any out-of-plane deformation in case it occurs. The readings of the strain gauges located at the same side of each column show consistent readings without significant variation in the values. The recorded strain values at the interior and exterior reinforcing bars are used to plot the strain profiles at the mid-height section of columns C1 through C4 at failure, as shown in Figs. 4.16 (a) through 4.16 (d), respectively.



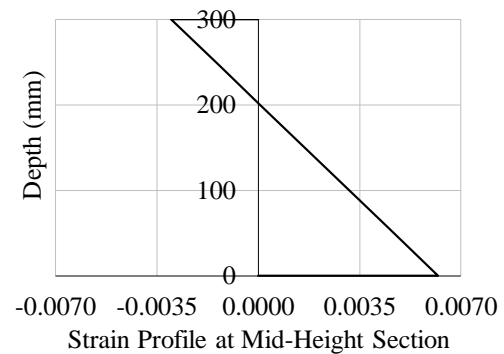
(a) Column C1



(b) Column C2



(c) Column C3



(d) Column C4

Figure 4.16: Strain Profile at Mid-Height Section of the Tested Columns.

The strain profiles show that failure of the tested columns occurs once the extreme compression fiber at the mid-height section reaches values between 0.0029 and 0.0033. It is worth mentioning that crushing of concrete is observed at the inner corner between the column and the cantilever in all examined columns. Theoretically, failure can occur at any section since the bending moment is uniform along the column's height. However, failure at the same location in all columns is attributed to the stress concentration in that area.

Another comparison reveals that varying the stainless-steel bars type has a minor influence on the strain profiles of the axially loaded members. For instance, changing the reinforcement type from Austenitic to Duplex results in an increase of curvature by just under 4.3% and 2.4% for the columns reinforced with 10-15M and 12-20M bars, respectively. Also, the same change causes an increase in the strain of the tension bars by about 17.3% and 10.1%, respectively. Thus, in the tested columns, using Duplex stainless-steel bars has a slight influence on improving the ductility of the member.

In both Austenitic and Duplex RC columns, the ultimate strain in the reinforcing bars subjected to tension decreases as the reinforcement ratio increases. This indicates that increasing reinforcement ratio in the examined stainless-steel RC columns results in an increase in capacity on the expense of ductility. For instance, changing the reinforcement from 10-15M to 12-20M results in a reduction of the ultimate strain in the tension bars by 30.6% and 21.3% for Austenitic and Duplex stainless-steel bars, respectively.

The load-strain curves at mid-height section of column C4 are shown in Fig. 4.17 for bars located at both faces of the column. The load-strain curve of the tension bars has the same trend of the load-deflection curve. The curve starts with a small slope in the pre-crack region followed

by an increase in slope after cracking occurs. For the inner reinforcing bars, compressive strains are detected at all loading values until crushing of concrete occurs at an ultimate strain in the compression bars of 0.0013. This value corresponds to a strain in the extreme compression fiber of 0.0031. As mentioned previously, these strains are measured at the mid-height section; whereas, crushing of concrete is observed at the top of the column.

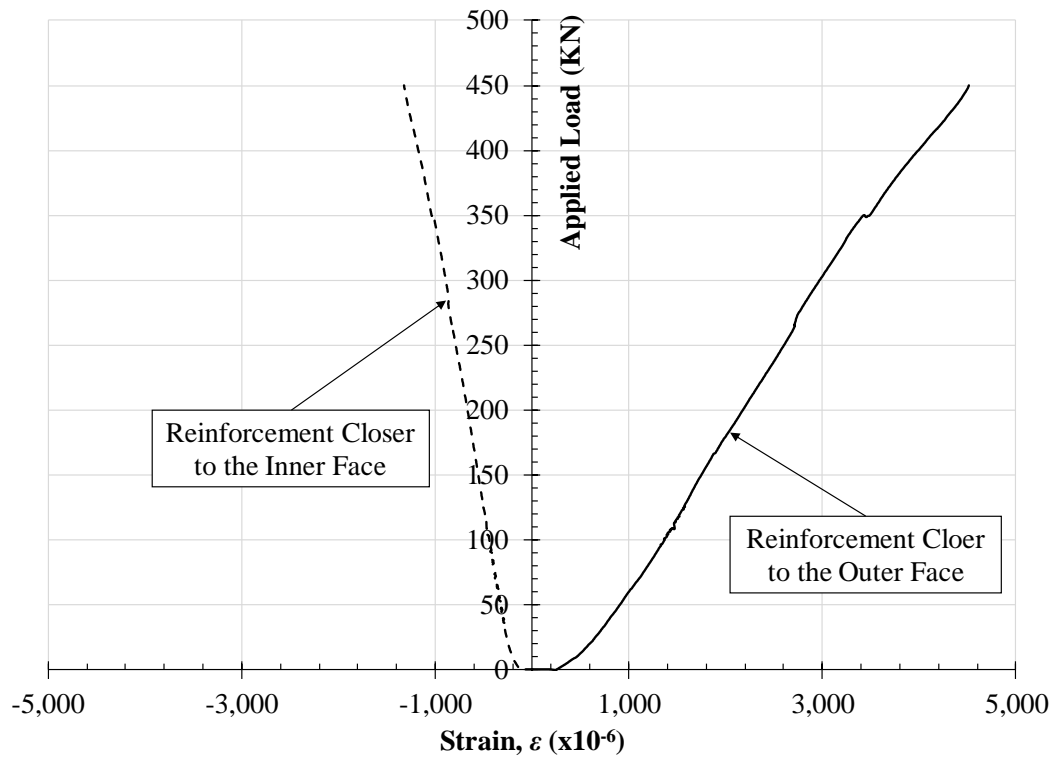


Figure 4.17: Variation of Strain in the Bars with Deflection at the Mid-Height Section

4.4. Analytical Model

An analytical model is developed based on the sectional analysis method to determine the strength and flexural deformation behavior of stainless-steel RC members subjected to different axial load levels. The mechanical properties and material models are considered based on the

compression tests performed on the concrete cylinders and the tensile tests performed on the stainless-steel bars. The following subsections discuss the assumptions, material models, and sectional analysis method in more details.

4.4.1. Assumptions

Assumptions considered in the analytical model includes the following:

- 1- Plane sections remain plane after deformation.
- 2- Perfect bond exists between concrete and the embedded stainless-steel bars.
- 3- Geometrical non-linearity is not considered.
- 4- Sufficient vertical reinforcement is provided to prevent shear failure.
- 5- Failure is defined when the extreme compression fiber reaches a strain value of 0.0035 as defined by CSA A23.3-14 [1].

4.4.2. Material Models

The behavior of both concrete and stainless-steel bars is considered using the models discussed in this subsection.

4.4.2.1. Concrete

The constitutive relationship proposed by Scott *et al.* [9] is adopted in the analytical model to describe the behavior of concrete in compression. The model provides a robust yet simple expression of the actual behavior of normal strength concrete. The compressive strength and the corresponding strain are obtained experimentally by performing compressive tests on concrete cylinders. Scott *et al.* model is shown in equation 4.1.

$$f_c = f'_c \left[2.0 \left(\frac{\varepsilon_c}{\varepsilon_o} \right) - \left(\frac{\varepsilon_c}{\varepsilon_o} \right)^2 \right] \quad (4.1)$$

Where f_c is concrete stress (MPa) corresponding to a strain value of ε_c ; f'_c is concrete compressive strength (MPa); and ε_o is the strain at peak stress. The tangential Young's modulus of concrete is taken as the first derivative of the concrete stress (f_c) with respect to its strain (ε_c) [1]. Concrete is assumed to have negligible tensile strength and tension stiffening behavior at all loading stages. Concrete stress-strain relationship is assumed to stop at the peak stress value since experimental tests were load controlled and stopped after failure mode. Effect of confinement reinforcement is considered as discussed in section 2.3.2.

4.4.2.2. Stainless Steel Bars

The results obtained from the tensile tests on the Austenitic and Duplex Stainless-Steel bars are utilized in the analytical program. Mathematical expressions are derived from the experimental data using polynomial curve fitting as a function of the bar type and size. The proposed expressions are shown in Appendix A.

4.4.3. Sectional Analysis

The load-deflection relationship and deformation behavior of the stainless-steel RC members are considered in view of the sectional analysis method [10-12]. The cross-section of each member is divided into several horizontal layers with a maximum thickness of 3.0 mm, which is found to result in adequate accuracy based on a preliminary sensitivity analysis. Strength analysis is performed by dividing the cross-section into multiple horizontal layers as shown in Fig. 4.18. The kinematic and compatibility conditions are considered in each layer based on the corresponding mechanical properties and stress-strain relationships of both concrete and stainless-steel bars.

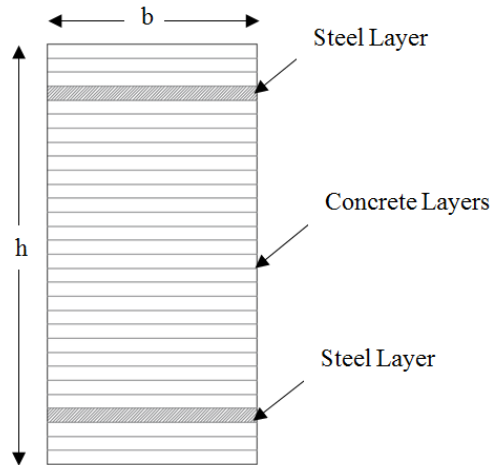


Figure 4.18: Typical Mesh for the Sectional Analysis Method

The analysis is performed in two stages. Firstly, the axial strain is increased incrementally, and the corresponding axial load is calculated by satisfying the equilibrium conditions. The process is repeated until the desired axial load is reached. After that, an incremental curvature is applied and the strain at each layer is calculated based on its location from the centroid. The applied curvature is increased gradually until failure occurs by crushing of concrete at the extreme compression fibers. Other failure modes are checked to ensure that they do not govern.

After obtaining the moment-curvature diagram, the moment-area method is used to determine the load-deflection curve. In case of the simply-supported beams, the load-deflection curve is obtained at the mid-span section based on a one-point loading scheme. In case of columns, the lateral deflection at the mid-height section of the column is obtained as a function of the applied load at the end of the cantilever.

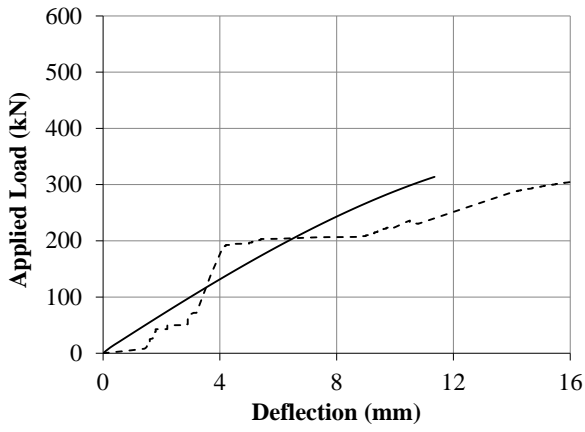
4.5. Validation of the Analytical Model

The capability of the proposed model to predict the strength and deformation behavior of stainless-steel RC members is validated in view of the obtained experimental results. The geometrical characteristics and mechanical properties of the tested specimens are detailed in Section 4.3.2 for beams B1 through B4, and Section 4.3.3 for columns C1 through C4.

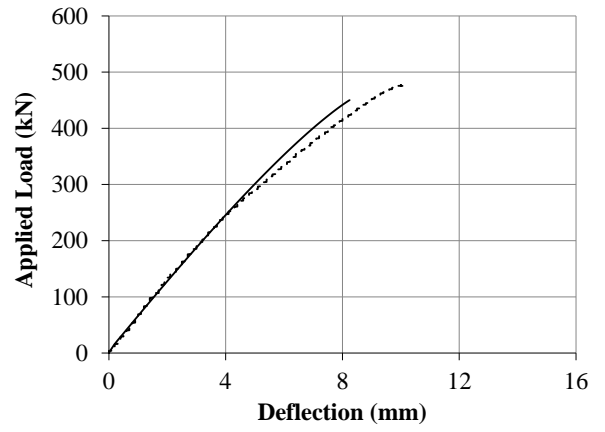
In general, the results obtained from the proposed model are found to be in a very good agreement with the experimental results.

4.5.1. Beams

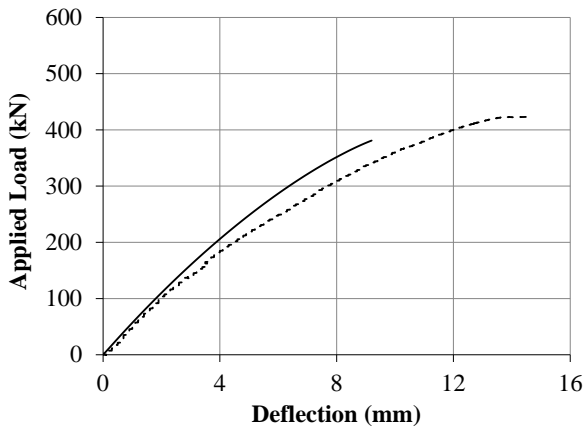
A comparison between the experimental and analytical load-deflection curves for beams B2 through B4 are shown in Figs. 4.19 (a) through 4.19 (c), respectively. In general, both curves share the same trend at the different loading conditions. The proposed model predicts the flexural capacity of all beam with very good accuracy as indicated by the calculated percent difference of 1.7%, 3.4%, 5.2% and 6.3% for beams B1 through B4, respectively. Regarding the flexural stiffness, a comparison is made to determine the percent difference of the secant stiffness at a loading value of 200 kN. A good match is shown between the analytical and experimental values as indicated by the percent difference of 4.3%, 5.4% and 6.3% for beams B2 through B4, respectively.



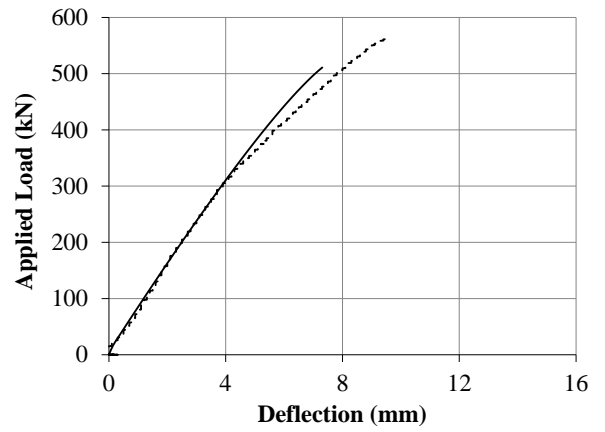
(a) Beam 1



(b) Beam 2



(c) Beam 3



(d) Beam 4

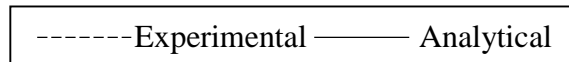
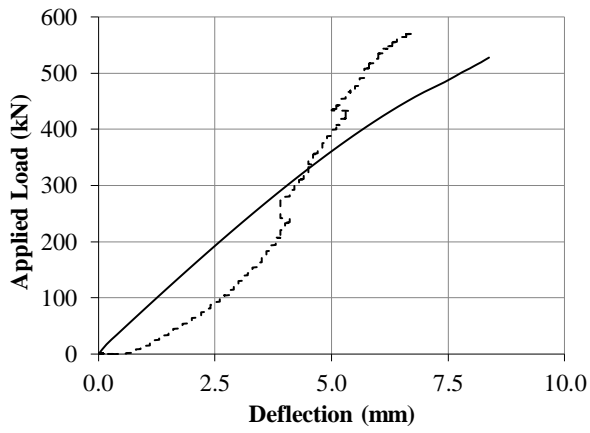


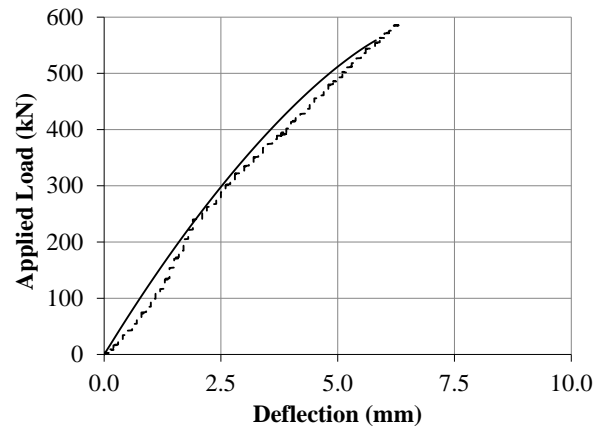
Figure 4.19: Validation of the Proposed Analytical Model with the Experimental Results

4.5.2. Columns

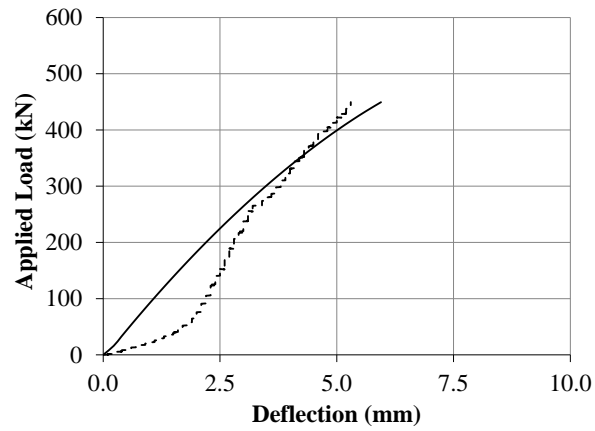
A similar comparison is conducted between the experimental and analytical load-deflection curves of columns C1, C2 and C4 as illustrated in Figs. 4-20 (a) through 4-20 (c), respectively. The comparison shows that the proposed model can predict the ultimate capacity of the examined columns with high accuracy as indicated by the percent difference of 5.5%, 4.7% and 1.1% for columns C1, C2 and C4, respectively. In terms of the shape of the load-deflection curves, there is a very good agreement as both the experimental and analytical curves cover the same range in the chart. However, the analytical results do not show the smaller slope at the beginning of the curve since the tensile strength of concrete is neglected in the analysis.



(a) Column 1



(b) Column 2



(c) Column 4

-----	Experimental	————	Analytical
-------	--------------	------	------------

Figure 4.20: Validation of the Proposed Analytical Model with the Experimental Results

4.6. Parametric Study

A parametric study is conducted based on the validated model to investigate the influence of the stainless-steel bars type, cross-sectional dimensions and reinforcement ratio on the stress developed in the stainless-steel bar at ultimate moment. Three values for each parameter are considered based on practical considerations. Thus, 27 cases are analyzed for each stainless-steel bar type for a total of 54 cases. The cross-sectional dimensions and reinforcement ratio of the 27 specimens are detailed in Table 4.3. The considered cross-sectional width (b) and height (h) are taken as 300 mm, 650 mm and 1000 mm. The reinforcement ratio of the main bars (ρ) is calculated for each section based on the minimum, average and maximum values given in the Canadian Highway Bridge Design Code [13]. The minimum reinforcement results in a flexural moment resistance that is at least 1.2 times the cracking moment, and the maximum reinforcement corresponds to a compression zone that does not exceed half the section height. Failure is considered once the extreme compression fiber in concrete reaches a strain value of 0.0035 [1].

Table 4.3: Dimensions and Reinforcement Ratios of the Beam Specimens

Specimen No.	Reinforcement Ratio	b (mm)	h (mm)	
1	Minimum	300	300	
2			650	
3			1000	
4		650	1000	300
5				650
6				1000
7		1000	1000	300
8				650
9				1000
10	Average	300	300	
11			650	
12			1000	
13		650	1000	300
14				650
15				1000
16		1000	1000	300
17				650
18				1000
19	Maximum	300	300	
20			650	
21			1000	
22		650	1000	300
23				650
24				1000
25		1000	1000	300
26				650
27				1000

Similarly, another parametric study is conducted on a different set of specimens to determine the influence of stainless-steel bars type, cross-sectional dimensions, reinforcement ratio and axial load level on the developed stresses in the stainless-steel bars. The cross-sectional width (b) and height (h) of the examined specimens are taken as 300 mm, 650 mm and 1000 mm. The reinforcement ratio (ρ) of the longitudinal steel bars is considered as 2.0%, 3.0% and 4.0% of

the cross-sectional area. The axial load level (λ) is set to 0.1 and 0.2. The axial load level is calculated as the ratio of the applied axial load to the axial capacity of the column. These calculations are embedded in the proposed analytical model. Table 4.4 provides a description of each of the 27 specimens for each load level and stainless-steel bar type. Thus, a total of 108 cases are considered in the parametric study of the column specimens.

Table 4.4: Dimensions and Reinforcement Ratio of the Column Specimens

Specimen No.	Reinforcement Ratio	b (mm)	h (mm)
C1	0.02	300	300
C2			650
C3			1000
C4		650	300
C5			650
C6			1000
C7		1000	300
C8			650
C9			1000
C10	0.03	300	300
C11			650
C12			1000
C13		650	300
C14			650
C15			1000
C16		1000	300
C17			650
C18			1000
C19	0.04	300	300
C20			650
C21			1000
C22		650	300
C23			650
C24			1000
C25		1000	300
C26			650
C27			1000

4.7. Effect of the Examined Parameters on Stainless-Steel RC Beams

The following subsections illustrate the influence of the examined parameters on the developed stress in the stainless-steel bars f_{ss} at ultimate load. The discussion takes into consideration the stainless-steel bar type, cross-sectional dimensions and reinforcement ratio with reference to Fig. 4.21.

4.7.1. Effect of Section Height (h)

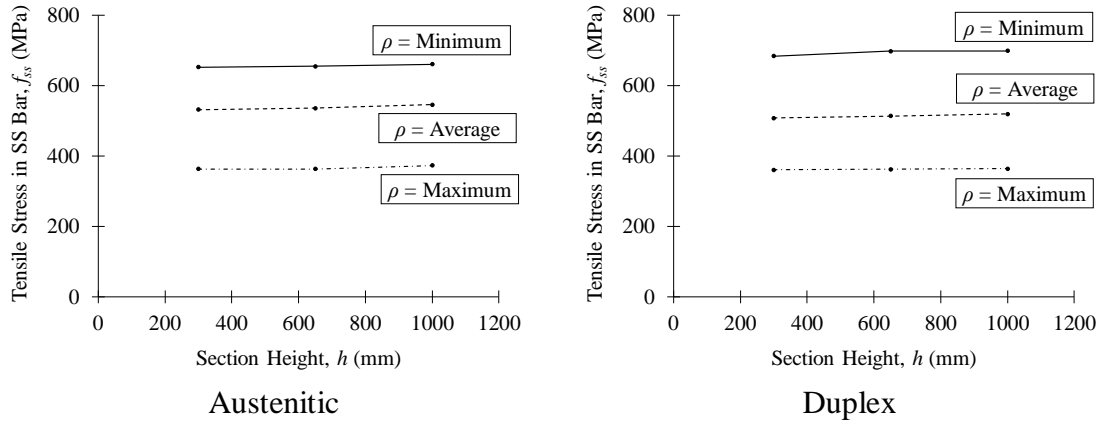
The influence of varying the cross-sectional height (h) on the stresses developed in the stainless-steel bars (f_{ss}) at failure is discussed in view Fig. 4.21(a). The results reveal that for the same reinforcement ratio, height variation has a negligible influence on f_{ss} . Increasing the height has a direct relationship with the area of the compression block and the lever arm between the tension steel bars and the centroid of the concrete compression block. Therefore, the increase in stiffness and flexural capacity is attributed to the increase in these factors; whereas, the stresses in the stainless-steel bars remain almost constant. However, changing the amount of the steel bars is found to have a significant impact on the stresses developed in the stainless-steel bars. For instance, increasing the reinforcement ratio from the minimum to the average value results in a drop in f_{ss} by 18.4% and 25.6% for Austenitic and Duplex stainless-steel RC members, respectively. Similarly, increasing the reinforcement ratio from the average calculated value to the maximum value results in a drop in f_{ss} by another 31.8% and 28.9% for the same bar types, respectively.

4.7.2. Effect of Section Width (b)

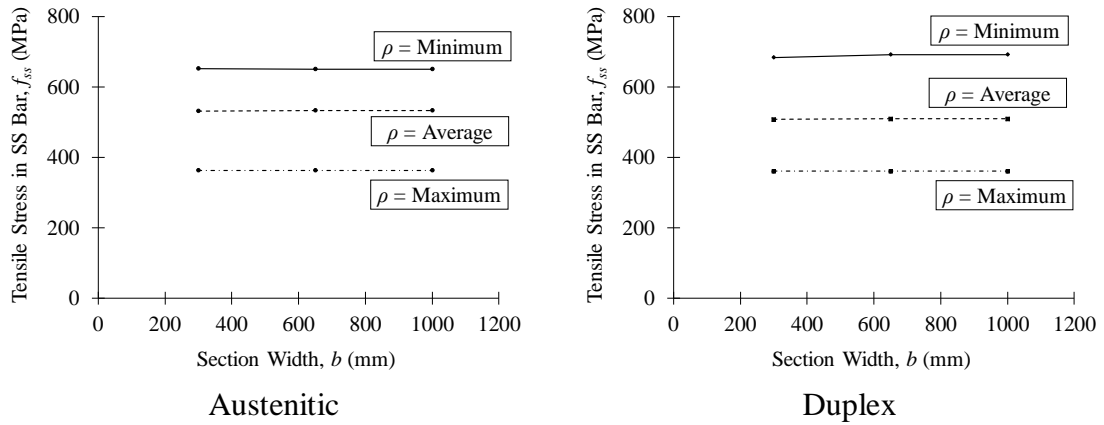
The effect of changing beam width (b) on the ultimate stress reached in the main reinforcement (f_{ss}) is illustrated in Fig. 4.21(b) for Austenitic and Duplex stainless-steel bars. For the same reinforcement ratio, the results show that increasing the section width from 350 mm to 1000 mm has a negligible impact on f_{ss} . The increase in stiffness and ultimate capacity is attributed to the larger compression block area associated with the wider section. However, by increasing the reinforcement ratio, the stresses in the stainless-steel bars decrease since crushing of concrete occur at lower curvature values. For example, changing the reinforcement ratio from minimum to average results in a drop by about 18.6% and 25.6% for Austenitic and Duplex stainless-steel bars, respectively. Also, changing the reinforcement ratio from average to minimum results in additional drop of 31.6% and 28.9% for the same bar types, respectively.

4.7.3. Effect of Reinforcement Ratio (ρ)

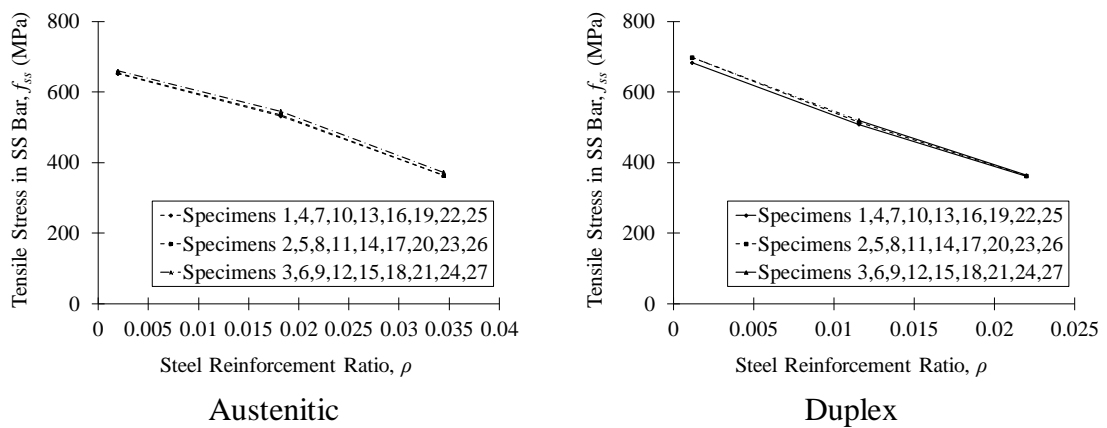
The influence of varying the reinforcement ratio of the main stainless-steel bars on the value of f_{ss} was discussed in Sections 4.7.1 and 4.7.2. To further illustrate the behavior, Fig. 4.21(c) is plotted considering all examined specimens. As shown in the figure, changing the cross-sectional dimensions at any reinforcement ratio does not alter the stresses in the stainless-steel bars significantly. However, as the reinforcement ratio increases, the ultimate stress in the stainless-steel bars decreases in an almost linear trend. The rate at which this drop occur is about 56% and 52% within the examined reinforcement ratios for Austenitic and Duplex stainless-steel bars, respectively.



(a) Section Height



(b) Section Width



(c) Steel Reinforcement Ratio

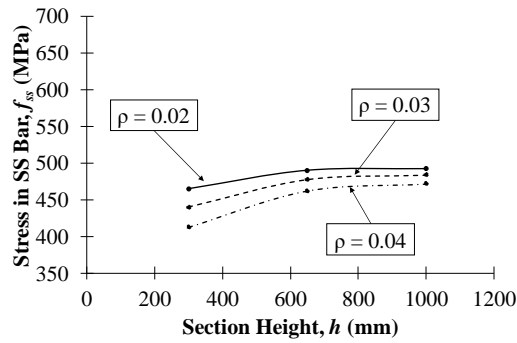
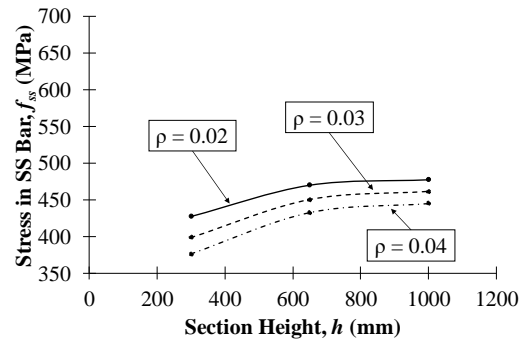
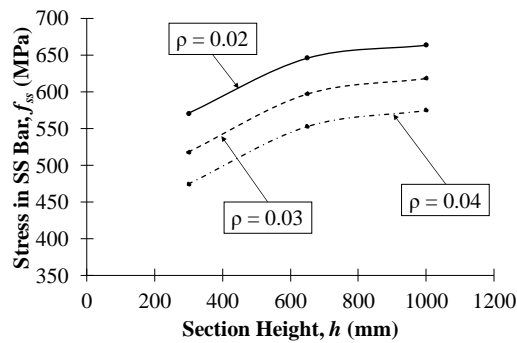
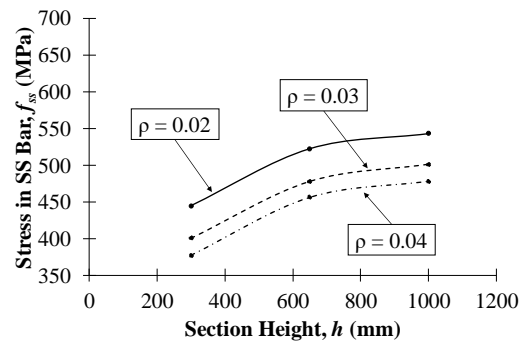
Figure 4.21: Influence of Various Parameters on the Tensile Stress in the SS Bars at M_R

4.8. Effect of the Examined Parameters on Stainless-Steel RC Columns

In the following subsections, the effect of varying the stainless-steel type, cross-sectional dimensions, reinforcement ratio and axial load level on the ultimate stress developed in the stainless-steel bars (f_{ss}) are discussed in view of Figs. 4.22 through 4.24. The specimens are subjected to an axial load level of either 0.1 or 0.2 followed by the application of incremental bending moment until failure occurs.

4.8.1. Effect of Section Height (h)

The influence of changing the section height (h) on the developed stresses in the stainless-steel bars (f_{ss}) in both Austenitic and Duplex stainless-steel RC columns under different axial load levels is illustrated in Fig. 4.22. In general, increasing the section height results in a consequent increase in f_{ss} . The rate of this increase depends on the stainless-steel bar type, the axial load level and the reinforcement ratio. For instance, in Austenitic bars subjected to an axial load level of 0.1, as section height increases from 300 mm to 1000 mm the rate of increase of f_{ss} varies between 5.9% and 14.3% for $\rho = 0.02$ and 0.04, respectively. By increasing the axial load level to 0.2, the rate of increase becomes higher as it ranges between 11.7% and 18.4% for the same reinforcement ratios, respectively. In Duplex stainless-steel bars, this observation becomes more evident as indicated by the higher rates of increase that vary between 16.4% and 21.2% at $\lambda = 0.1$, and between 22.2% and 26.8% at $\lambda = 0.2$. The flexural capacity increases in axially loaded members as the section height increases due to the larger lever arm to the centroid of the section. Also, the curvature increases causing the strains and consequently the stresses in the tension reinforcement to increase.

(a) Austenitic ($\lambda = 0.1$)(b) Austenitic ($\lambda = 0.2$)(c) Duplex ($\lambda = 0.1$)(d) Duplex ($\lambda = 0.2$)**Figure 4.22: Influence of Varying h on f_{ss} in Stainless-Steel RC Columns**

4.8.2. Effect of Section Width (b)

A similar analysis is performed considering the influence of varying the section width (b) on the value of f_{ss} as illustrated in Fig. 4.23. As shown in the figure, the section width has a negligible effect on the stress developed in the bars corresponding to the ultimate load regardless of the axial load level or the reinforcement ratio for both bar types. Increasing the section width results in increasing the flexural capacity due to the wider compression block. However, the curvature of the section at ultimate load is not influenced significantly. Therefore,

the strains and the corresponding stresses in the reinforcing bars are not significantly affected. For each bar type, increasing the reinforcement ratio causes a reduction in f_{ss} since the member reaches its ultimate capacity at a lower curvature value. This reduction is more pronounced in Duplex stainless-steel bars as they have higher strength compared to the Austenitic bars. For instance, at an axial load level of 0.1, increasing the reinforcement ratio from 0.02 to 0.04 results in a reduction of f_{ss} value by 5.7% and 14.4% in the Austenitic and Duplex bars, respectively.

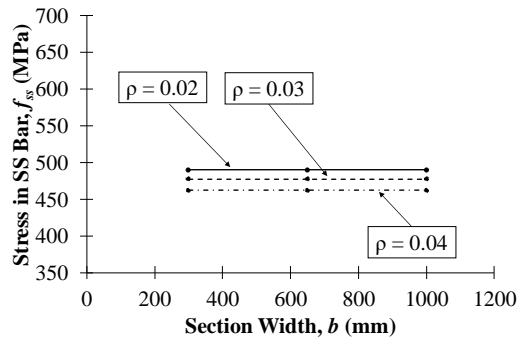
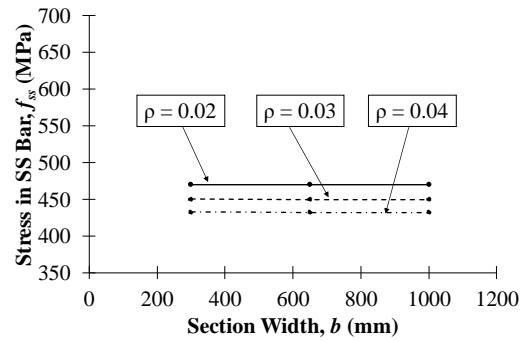
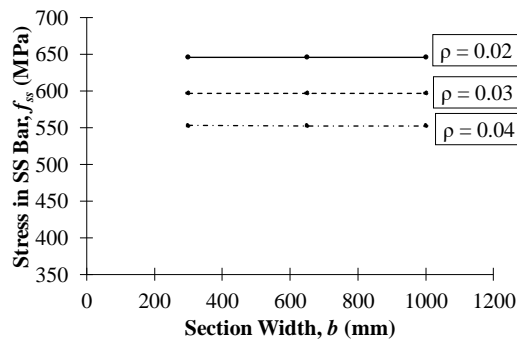
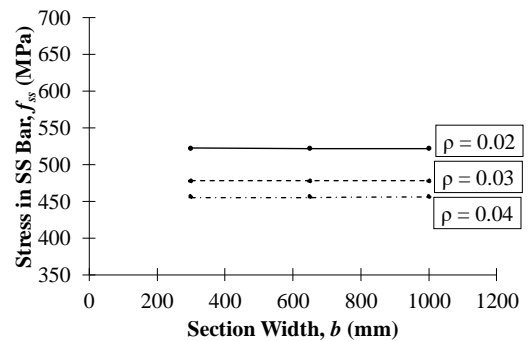
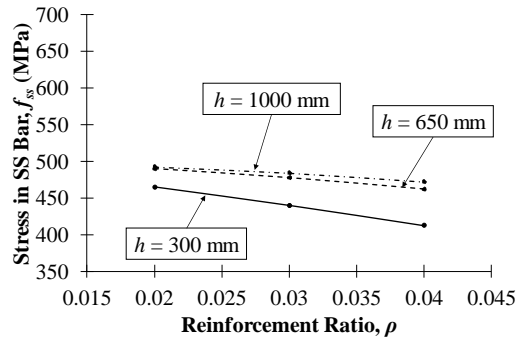
(a) Austenitic ($\lambda = 0.1$)(b) Austenitic ($\lambda = 0.2$)(c) Duplex ($\lambda = 0.1$)(d) Duplex ($\lambda = 0.2$)

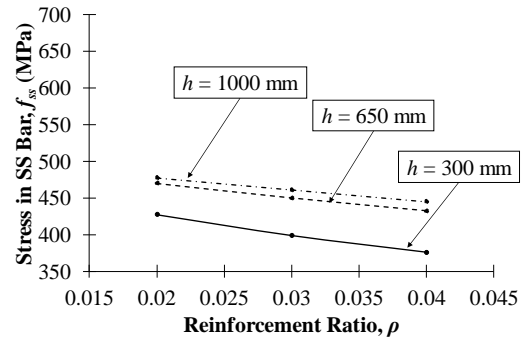
Figure 4.23: Influence of Varying b on f_{ss} in Stainless-Steel RC Columns

4.8.3. Effect of Reinforcement Ratio (ρ)

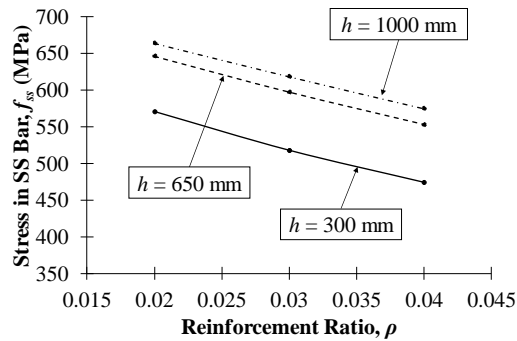
The effect of changing the reinforcement ratio on f_{ss} was discussed in Sections 4.8.1 and 4.8.2. The variation of f_{ss} with ρ is shown in Fig. 4.24 for both bar types at different axial load level. Each set of curves is plotted considering all specimens. In general, increasing the reinforcement ratio results in reducing f_{ss} since the ultimate capacity is reached at a smaller curvature. This indicates the member becomes less ductile as the reinforcement ratio increases. Section height has a remarkable impact on the f_{ss} values but a slight influence on the rate at which f_{ss} decreases with the reinforcement ratio.



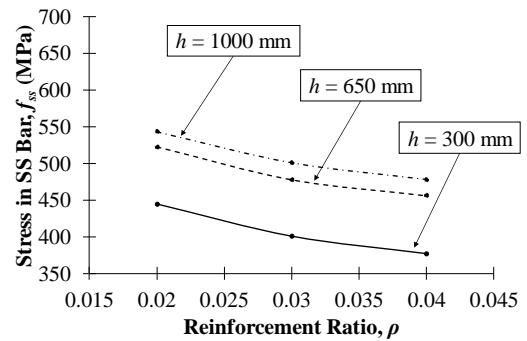
(a) Austenitic ($\lambda = 0.1$)



(b) Austenitic ($\lambda = 0.2$)



(c) Duplex ($\lambda = 0.1$)



(d) Duplex ($\lambda = 0.2$)

Figure 4.24: Influence of Varying ρ on f_{ss} in Stainless-Steel RC Columns

4.9. Proposed Procedure to Calculate the Flexural Capacity of Stainless-Steel RC Members

The application of the CSA A23.3-14 [1] procedure to calculate the flexural capacity of stainless-steel RC members has to take into account the yield stress of the reinforcing bars. Since stainless-steel bars lack a well-defined yield plateau, an equivalent stress has to be evaluated in order to establish the equilibrium condition in the CSA A23.3-14 [1] procedure. This study proposes a method in view of the validated parametric study to determine the equivalent stress (f_{ss}) of both Duplex and Austenitic stainless-steel bars.

Regression analysis is implemented to determine the best-fit equation that describes the relationship between the equivalent stress and the investigated parameters. For beams, the value of the equivalent yield stress is found to be highly correlated to the reinforcement ratio (ρ). The influence of the section cross-sectional dimensions and concrete mechanical properties are found to be negligible. Based on that, Equations (4.2a) and (4.2b) are proposed to calculate f_{ss} for Austenitic and Duplex stainless-steel bars, respectively.

$$f_{ss} = -102063\rho^2 - 5196\rho + 666.59 \geq 360 \text{ MPa} \quad \text{for Austenitic 316LN} \quad (4.2a)$$

$$f_{ss} = 56611\rho^2 - 12308\rho + 719.11 \geq 360 \text{ MPa} \quad \text{for Duplex 2205} \quad (4.2b)$$

In a similar manner, regression analysis is considered to determine expressions to calculate the equivalent stress in axially loaded members. The axial load level (λ) is limited to a maximum of 0.2 to match the examined range in the parametric study. The limits of the cross-sectional dimensions range from 300 mm to 1000 mm. The longitudinal steel reinforcement ratio is limited to a maximum of 4.0%. The proposed method assumes a linear strain profile along the

cross-section. The reinforcing bars located to one side of the neutral axis are subjected to compressive stresses; whereas the remaining bars located at the other side are subjected to tensile stresses. The proposed expressions account for this variation when calculating the equivalent stress at failure (f_{ss}). Equations (4.3a) and (4.3b) are proposed to calculate f_{ss} for Austenitic and Duplex stainless-steel bars, respectively:

$$f_{ss} = 500.0 - 568.9 \rho - 95.9 \lambda - 0.0093 h \quad \text{for Austenitic 316LN (4.3a)}$$

$$f_{ss} = 704.4 - 1067.8 \rho - 580 \lambda + 0.082 h \quad \text{for Duplex 2205 (4.3b)}$$

The calculation procedure for the flexural capacity of the stainless-steel RC members relies on the axial load level (λ) acting on the members. If $\lambda = 0$, then the member is considered a beam element and Equation 4.1 is used to calculate an equivalent yield stress, which will be substituted in the equilibrium equation according to CSA A23.3-14 [1]. However, if $0 < \lambda \leq 0.2$, then Equation 4.3 is used to calculate the stresses in the stainless-steel bars. Then, the equilibrium condition is established, and the corresponding flexural capacity is calculated. Examples illustrating the proposed procedure are provided in Appendix B.

The proposed simplified procedure is validated against the experimental results obtained from testing the beam and column specimens. The proposed procedure provides a very good prediction of the actual behavior of the stainless-steel bars as shown in Figs. 4.25 and 4.26. A comparison between the proposed equation and the experimental results reveal a very good agreement as indicated by average errors of 3.9% and 5.7% for the beam and column specimens, respectively. The negligible presence of outliers results in a higher confidence in the proposed procedure. The comparison between the experimental results and the current 0.2%

offset method revealed an average error of 8.0% and 11.8% for the beam and column specimens, respectively.

The proposed procedure was also validated against the analytical results obtained from parametric study in Fig. 4.27. The line of equality plot for all specimens reveal that the proposed procedure provides a better approximation of the moment of resistance of stainless-steel RC sections than the current 0.2% offset method. The proposed equation revealed an average error of 3.7% and 4.8% for beams and columns, respectively, while the current 0.2% offset method indicated an average error of 24.3% and 14.1% for beams and columns, respectively.

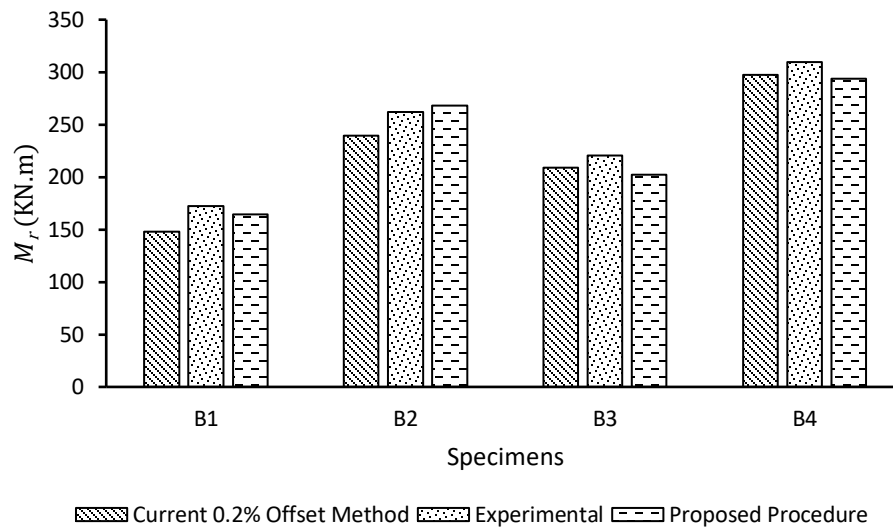


Figure 4.25: Accuracy of Predicting M_R for Experimentally Tested Beams

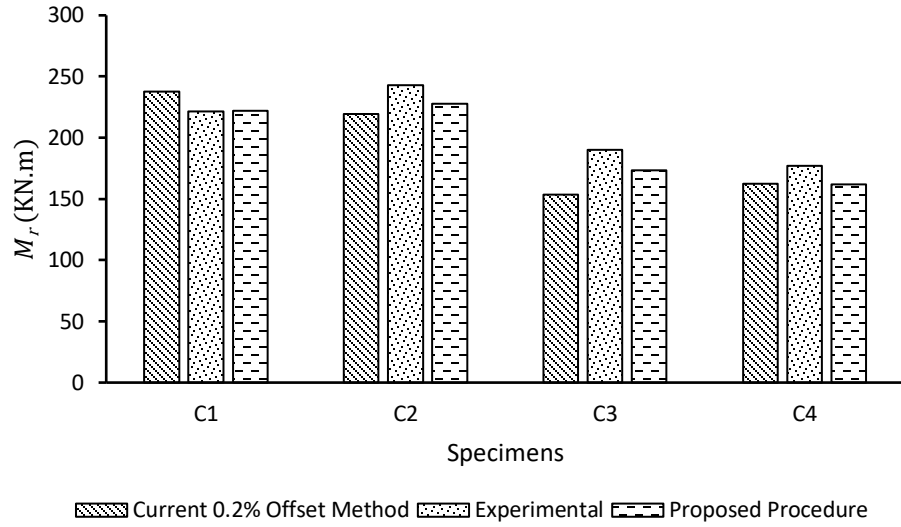


Figure 4.26: Accuracy of Predicting M_R for Experimentally Tested Columns

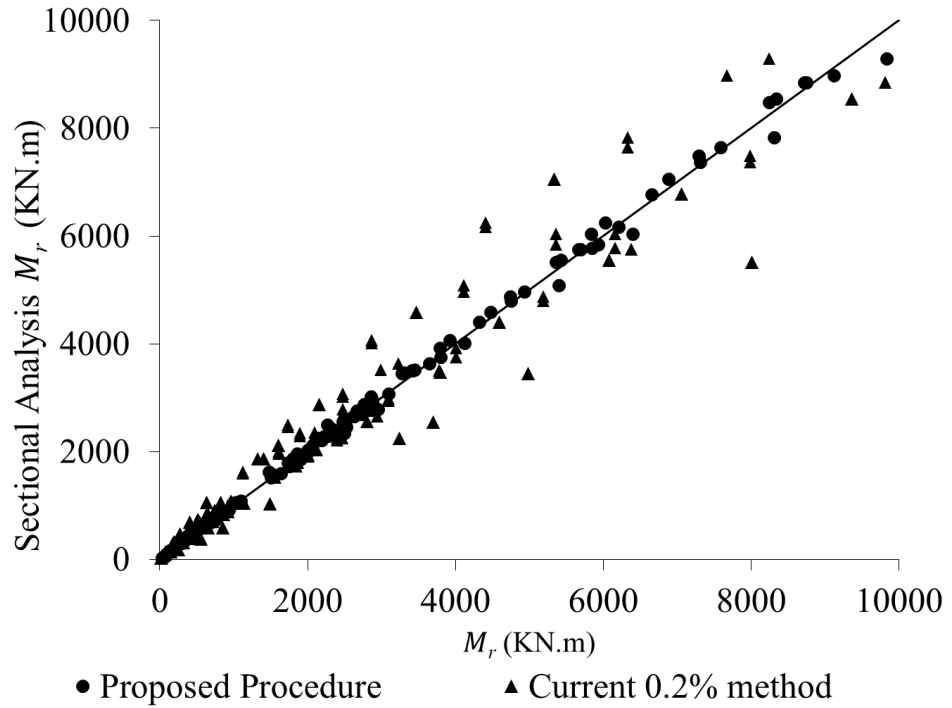


Figure 4.27: Accuracy of M_R for Parametric Study Sections

4.10. Summary and Conclusions

The current chapter provided a description of the experimental and analytical programs that were carried out to evaluate the behavior of stainless-steel RC members and to propose a procedure to calculate their flexural capacity. The study commenced by performing tensile tests on both Austenitic and Duplex stainless-steel bars to determine their mechanical properties and actual constitutive relationships. After that, four large scale stainless-steel RC beams were tested in a one-point loading scheme to assess their flexural performance. Additional tests are conducted on four eccentrically loaded large-scale columns to investigate their deformation behavior and failure mode. An analytical model was then proposed and validated based on the experimental results. The validated model is utilized to perform a parametric study to investigate the influence of varying the cross-sectional dimensions, reinforcement ratio, stainless-steel type and axial load level on the stresses (f_{ss}) developed in the bars at ultimate load. A total of 54 cases for beams and 108 cases for columns were examined. The results revealed that reinforcement ratio and axial load level are the main factors affecting the value of f_{ss} . The influence of section height becomes more pronounced as the axial load level increases; whereas section width was found to have a negligible impact on the value of f_{ss} . Finally, a regression analysis was performed to propose mathematical expressions of the equivalent stress (f_{ss}), which can be used to calculate the flexural capacity stainless-steel RC members.

Appendix A

1) Duplex 15mm:

$$\begin{aligned}\sigma = & -521248304587\varepsilon^6 + 126305323287.875\varepsilon^5 - 12028601923.7344\varepsilon^4 \\ & + 570123288.367676\varepsilon^3 - 14030445.612732\varepsilon^2 + 169861.877162\varepsilon \\ & - 7.969042\end{aligned}$$

$$\begin{aligned}E = & (-3.127489828 * 10^{12})\varepsilon^5 + (6.315266164 * 10^{11})\varepsilon^4 - (4.811440769 * 10^{10})\varepsilon^3 \\ & + 1710369865\varepsilon^2 - 28060891.23\varepsilon + 169861.877162\end{aligned}$$

2) Duplex 20mm:

$$\begin{aligned}\sigma = & -1783680347086\varepsilon^6 + 346499807212.743\varepsilon^5 - 26282819168.9342\varepsilon^4 \\ & + 982862922.255052\varepsilon^3 - 18825735.43222\varepsilon^2 + 174780.778805\varepsilon \\ & - 0.432424\end{aligned}$$

$$\begin{aligned}E = & (-1.070208208 * 10^{13})\varepsilon^5 + (1.732499036 * 10^{12})\varepsilon^4 - (1.051312767 * 10^{11})\varepsilon^3 \\ & + 2948588767\varepsilon^2 - 37651470.86\varepsilon + 174780.778805\end{aligned}$$

3) Austenitic 15mm:

$$\sigma = -5667627300.04492\varepsilon^3 + 19144901.559034\varepsilon^2 + 128450.543324\varepsilon - 1.908335$$

$$E = (-1.70028819 * 10^{10})\varepsilon^2 + 38289803.12\varepsilon + 128450.543324$$

If $\varepsilon > 0.003475$:

$$\sigma = 1961.1\varepsilon + 465.2$$

$$E = 1961.1$$

4) Austenitic 20mm:

$$\begin{aligned}\sigma = & 72714412816640\varepsilon^6 - 5903055587389\varepsilon^5 + 170784892289.319\varepsilon^4 \\ & - 1890532909.02249\varepsilon^3 - 174236.315782\varepsilon^2 + 142575.102797\varepsilon \\ & + 3.526021\end{aligned}$$

$$\begin{aligned}E = & (4.362864769 * 10^{14})\varepsilon^5 - (2.951527794 * 10^{13})\varepsilon^4 + (6.831395692 * 10^{11})\varepsilon^3 \\ & - 5671598727\varepsilon^2 - 348472.6316\varepsilon + 142575.102797\end{aligned}$$

5) Austenitic 30mm:

$$\sigma = -7959649755.82422\varepsilon^3 + 19308066.100039\varepsilon^2 + 146086.480857\varepsilon + 0.523437$$

$$E = (-2.387894927 * 10^{10})\varepsilon^2 + 38616132.2\varepsilon + 146086.480857$$

if $\varepsilon > 0.003687$:

$$\sigma = 2461.2\varepsilon + 414.08$$

$$E = 2461.2$$

Appendix B

Example 1 - Beam B2:

- **Concrete section properties:**

h (Section height) = 400 mm,

A_s (Steel Area) = 2100 mm²,

b (Section width) = 250 mm,

f_c' (Concrete compressive strength) = 35 MPa,

c (concrete cover) = 35 mm,

d (Stainless steel bar diameter) = 30 mm,

Φ (Stirrup diameter) = 10 mm

- **Calculation Procedure:**

1. Calculate Section depth:

$$Depth = h - c - \Phi - 0.5d = 340mm$$

2. Calculate Section reinforcement ratio.

$$\rho = \frac{A_s}{bg} = 0.024706$$

3. Calculate proof stress using proposed equation:

$$f_{ss} = -102063\rho^2 - 5196\rho + 666.59 = 475.92 MPa.$$

4. Calculate Reinforcement Tensile Force:

$$T_s = f_{ss} * A_{SS} = 999434 N$$

5. Calculate ratio of equivalent concrete compressive stress developed under flexure to concrete cylinder:

$$\alpha = 0.85 - 0.0015f_c' = 0.7975.$$

6. Calculate rectangular neutral axis depth:

$$a = \frac{T_s}{\alpha b f_c'} = 143.22mm$$

7. Calculate Section moment of resistance:

$$M_r = T_s * \left(d - \frac{a}{2} \right) = 268.24 \text{ Kn. m.}$$

Example 2: Column C4:

• **Concrete section properties:**

Dimensions: 300*300 mm,

A_s (Steel Area) = 2000 mm²

f_c' (Concrete compressive strength) = 40 MPa,

c (concrete cover) = 35 mm,

d (Stainless steel bar diameter) = 15 mm,

Φ (Stirrup diameter) = 10 mm,

P_e (Experimental Axial Load) = 442.6 KN.

• **Calculation Procedure:**

1. Calculate Section reinforcement ratio.

$$\rho = \frac{A_s}{bh} = 0.02222$$

2. Calculate ratio of equivalent concrete compressive stress developed under flexure to concrete cylinder:

$$\alpha = 0.85 - 0.0015f_c' = 0.79.$$

3. Calculate section axial capacity.

$$P_c = \alpha f_c' (bh - A_s) + A_s f_{ss} = 2844 \text{ Kn}$$

4. Calculate Axial Load Level.

$$\lambda = \frac{P_e}{P_c} = 0.155626$$

5. Calculate proof stress for tension reinforcement:

$$f_{ss} = 704.4 - 1067.8 \rho - 580 \lambda + 0.082 h = 615.03 \text{ MPa}$$

6. Calculate proof stress for compression reinforcement:

$$f_{ss}' = 196 \text{ MPa. (Using stress-strain curve in Appendix A)}$$

7. Assume one row for tension reinforcement:

$$T_s = 0.5 * A_s * f_{ss} = 615053 \text{ N}$$

8. Assume one row for compression reinforcement:

$$C_s = 0.5 * A_s * f_{ss2} = 196000 \text{ N}$$

9. Calculate concrete compressive force.

$$C_c = f_c' \alpha a b = 762490 \text{ N}$$

10. Calculate section moment of resistance.

$$M_r = (T_s + C_s) * (0.5h - 55) + (C_c * (0.5h - 0.5a)) = 161.7188 \text{ Kn. m.}$$

4.11. References

- [1] CSA Group, 2014, Design of Concrete Structures (CSA A23.3-14), sixth edition, Ottawa, ON, 297 p.
- [2] Kazinczy, G. V., 1993, Die Plastizität des Eisenbetons, *Beton und Eisen*, 32 (5): 74-80.
- [3] Whitney, C. S., 1942, Plastic Theory in Reinforced Concrete Design, *Transactions, ASCE*, 107: 251-326.
- [4] Rasmussen, K.J.R., 2003. Full Range Stress–Strain Curves for Stainless Steel Alloys, *Journal of Constructional Steel Research*, 59: 47–61.
- [5] ASTM A370, 2014, Standard Test Methods and Definitions for Mechanical Testing of Steel Products, ASTM International, West Conshohocken, PA, USA, 50 p.
- [6] ASTM A276, 2017, Standard Specification for Stainless Steel Bars and Shapes, ASTM International, West Conshohocken, PA, USA, 8 p.
- [7] ASTM C39, 2018, Standard Test Method for Compressive Strength of Cylindrical Concrete Specimens, ASTM International, West Conshohocken, PA, USA, 8 p.
- [8] Zhou, K., Ho, J., and Su, R., 2011, Flexural Strength and Deformability Design of Reinforced Concrete Beams, *Procedia Engineering, Elsevier*, 14: 1399-1407.
- [9] Scott, B.D., Park, R. and Priestley, M.J.N., 1982, Stress-Strain Behavior of Concrete Confined by Overlapping Hoops at Low and High Strain Rates, *Journal of the American Concrete Institute*, 79 (1): 13-27.
- [10] Youssef, M.A., and Rahman M., 2007, Simplified Seismic Modeling of Reinforced Concrete Flexural Members, *Magazine of Concrete Research*, 59 (9): 639-649.
- [11] Alhadid, M.A., and Youssef, M.A., 2017, Analysis of Reinforced Concrete Beams Strengthened Using Concrete Jackets, *Engineering Structures, Elsevier*, 132: 172-187.
- [12] Alhadid, M.A., and Youssef, M.A., 2018, Assessment of the Flexural Behavior of Reinforced Concrete Beams Strengthened with Concrete Jackets, *Engineering Structures, Elsevier*, 167: 108-120.

- [13] CSA Group, 2014, Canadian Highway Bridge Design Code (CSA S6-14), eleventh edition, Ottawa, ON, 894 p.

Chapter 5

5. CONCLUSION

5.1. Summary

Thermal incompatibility between stainless-steel and concrete in stainless-steel reinforced concrete members raises a concern during the early ages, when heat of hydration induced stresses are at their peak. To analyze the behavior of stainless-steel reinforced concrete sections during the hydration process, a thermal-structural finite element model was developed. A transient thermal analysis determined the temperature distribution within concrete. Then, structural analysis determined the stress distribution inside concrete and stainless-steel radial expansion.

To study the flexural performance of stainless-steel RC members, an experimental-analytical program was carried out. In the first stage, Tensile tests were performed on both Duplex (2205) and Austenitic (316 LN) stainless-steel bars to determine their mechanical properties. In the second stage, four large scale stainless-steel RC beams were tested in a one-point loading scheme to investigate their failure mode and load-deflection relationship. Four tests are conducted on four eccentrically loaded short columns to evaluate their flexural behavior and strain distribution. In the third stage, an analytical model was then proposed and validated upon the experimental results. The validated model was utilized to carry out a parametric study to assess the effect of changing the axial load level, reinforcement ratio, cross-sectional dimensions, and stainless-steel type on the stresses developed in the bars at ultimate load. A total of 162 RC members were examined.

5.2. Conclusions

5.2.1. Properties of Stainless-Steel Reinforced Sections during Early Hydration Process

The developed finite element analysis on the early thermal expansion of stainless steel reinforced concrete sections concluded that the developed stresses due to the expansion of the SS bars did not result in concrete cracking. Additionally, the following findings were observed.

1. Maximum Temperature inside concrete is affected by the size of the specimen. It is not affected by SS bar diameter or type.
2. The diameter of the SS bar and the temperature generated from the hydration reaction in the concrete around it affect the value of the radial thermal expansion of SS.
3. Minimizing the temperature is important to control the radial expansion of SS bars during the first two days, as generated stresses are at their peak while the concrete strength is relatively small. Therefore, Continuous water curing of concrete reduces the principal stresses.
4. Using Duplex SS bars instead of austenitic SS bars minimizes the radial expansion of SS and the thermal stresses since it has less coefficient of thermal expansion.
5. Using water curing instead of air curing reduces thermal stresses radial thermal expansion of SS bars, and the maximum temperature inside concrete.
6. The diameter of the SS bar has a negligible effect on the radial thermal expansion of SS bars and the generated thermal stresses.

5.2.2. Flexural Performance of Stainless-Steel Reinforced Concrete Sections

Experimental and analytical programs were carried out to evaluate the strength behavior of stainless-steel RC members in order to propose a procedure to calculate their flexural capacity. It concluded that:

1. Increasing the reinforcement ratio in tested specimens resulted in the reduction of their ultimate deformation indicating that relationship between the flexural capacity of stainless steel RC sections and ductility is inversely proportional.
2. Section width was found to have a negligible impact on the value of f_{ss} since it had insignificant effect in the section curvature at ultimate load. Section height effect increased as the axial load level increases.
3. Reinforcement ratio is the main factor affecting the value of f_{ss} . Increasing the reinforcement ratio reduces the value of f_{ss} as the ultimate capacity is reached at smaller curvature.
4. Statistical analysis was performed to propose mathematical expressions of the equivalent stress (f_{ss}), which can be used to calculate the flexural capacity of austenitic and duplex stainless-steel RC members.
5. The proposed equations resulted in 3.9% and 5.74% average error with experimental results of beams and columns, respectively. In comparison, the current 0.2% method gave an 8.0% and 11.775% average error for beams and columns, respectively. The proposed procedure revealed an average error of 3.72% and 4.85% with analytical results of beams and columns, respectively. In comparison, the current 0.2% offset method resulted in an average error of 24.28% and 14.06% for beams and columns,

respectively. Results indicate that the proposed equations give a good approximation to the stainless-steel RC members flexural behavior.

5.3. Recommendations

Regarding the finite element model addressing the thermal characteristics of SS, the following recommendations are proposed for further research:

1. A parametric study on the thermal relation between concrete and stainless steel that involves the rapid hardening cement, the low heat cement and compare it with the findings based on the Ordinary Portland cement.
2. Expand the parametric study of reinforced concrete sections to involve specific applications, as: columns, beams and slabs.
3. Include viscous deformation of concrete at early ages in heat of hydration study.

Regarding the experimental and analytical model addressing the flexural capacity of stainless-steel RC sections, the following recommendations are proposed for further research:

1. Expand the range of tested and analyzed specimens to include long columns, slabs.
2. Develop mathematical expressions to calculate ferritic stainless-steel RC members flexural capacity.

CURRICULUM VITAE

Name: Mokhtar Khalifa

Post-secondary Education and Degrees: University of Alexandria
Alexandria, Alexandria, Egypt
2009-2014 B.A.

Related Work Experience

Structural Engineer
Al Quds Steel, Alexandria, Egypt
2016-2018

Teaching Assistant
The University of Western Ontario
2017-2018

Publications:

Khalifa, Mokhtar A., Alhadid, Monir M., Youssef, Maged A. (2018) “Early Age Thermal Expansion of Stainless-Steel Reinforced Concrete Sections”. Proceedings of the 10th International Conference on Short and Medium Span Bridges, Quebec City, Quebec, Canada.